

# Computational Discovery of Fast Interstitial Oxygen Conductors

Jun Meng<sup>1,4</sup>, Md Sariful Sheikh<sup>1,4</sup>, Ryan Jacobs<sup>1</sup>, Jian Liu<sup>2</sup>, William O. Nachlas<sup>3</sup>, Xiangguo Li<sup>1</sup>, Dane Morgan<sup>1,\*</sup>

<sup>1</sup> Department of Materials Science and Engineering, University of Wisconsin Madison, Madison, WI, USA.

<sup>2</sup> DOE National Energy Technology Laboratory, Morgantown, WV, USA.

<sup>3</sup> Department of Geoscience, University of Wisconsin Madison, Madison, WI, USA.

<sup>4</sup> These authors contributed equally: Jun Meng, Md Sariful Sheikh. E-mails: [ddmorgan@wisc.edu](mailto:ddmorgan@wisc.edu).

New highly oxygen-active materials may enhance many energy-related technologies by enabling efficient oxygen-ion transport at lower temperatures, e.g., below  $\approx 400$  °C. Interstitial oxygen conductors have the potential to realize such performance but have received far less attention than vacancy-mediated conductors. Here, we combine physically-motivated structure and property descriptors, *ab initio* simulations, and experiments to demonstrate an approach to discover new fast interstitial oxygen conductors. Multiple new families were found which adopt completely different structures from known oxygen conductors. From these families, we synthesized and studied oxygen kinetics in  $\text{La}_4\text{Mn}_5\text{Si}_4\text{O}_{22+\delta}$  (LMS), a representative member of perrierite/chevkinite family. We found LMS has higher oxygen ionic conductivity than the widely used yttria-stabilized  $\text{ZrO}_2$ , and among the highest surface oxygen exchange rates at intermediate temperature of known materials. The fast oxygen kinetics is the result of simultaneously active interstitial and interstitialcy diffusion pathways. We propose that the essential features for forming an effective interstitial oxygen conductor are the availability of electrons and structural flexibility enabling sufficient accessible volume. This work provides a powerful approach for understanding and discovering new interstitial oxygen conductors.

Materials which rapidly conduct oxygen are critical for a variety of energy devices such as fuel cells (solid oxide,<sup>1,2</sup> proton ceramic,<sup>3,4</sup> and reversible<sup>5</sup> cells), electrolyzers,<sup>6</sup> solid-oxide metal-air redox batteries,<sup>7</sup> gas sensors,<sup>8</sup> chemical looping devices,<sup>9</sup> memristors,<sup>10</sup> and oxygen separation membranes.<sup>11</sup> Almost all of the state-of-the-art oxygen-active materials transport oxygen through a vacancy-mediated mechanism, which typically only have adequate oxygen kinetics for practical applications at high temperatures  $\approx 800$  °C, impeding their use at lower temperatures desirable for more cost-effective and longer-lasting device operation. Vacancy-mediated conductors have dominated the science of oxygen-active materials for decades, resulting in many significant

discoveries related to oxygen vacancy conductors since the first such material, yttria-stabilized  $\text{ZrO}_2$ , was discovered.<sup>12–16</sup> In contrast, interstitial oxygen conductors are relatively uncommon and have received very limited study, despite having many potential advantages over vacancy-mediated conductors. First, interstitial oxygen conductors typically have lower migration barriers compared to vacancy oxygen conductors. This observation is supported by the experimental migration barriers for oxygen ion-conducting oxides in **Fig. 1**, where data sourced from the Citrine Informatics ARPA-E Ionics Database,<sup>17</sup> as well as recent literatures. (See details in **SI Discussion 1**). Although the database may have biases, e.g., due to the data collection or the available experimental studies, it is still

suggestive that it shows average migration barriers values of  $\approx 0.6$  eV versus  $\approx 1.1$  eV for interstitial and vacancy oxygen conductors, respectively. This  $\approx 0.5$  eV reduction in migration barrier would afford an approximate  $\times 1000$  increase in ionic conductivity at 600 °C. Second, at fixed  $P(\text{O}_2)$ , interstitial oxygen becomes thermodynamically more favorable as the temperature is decreased (i.e., more oxidizing conditions). This higher defect concentration will increase the oxygen conductivity at low temperatures, opposite the trend in vacancy conductors. Third, interstitial oxygen may exhibit a tendency of increasing rather than decreasing diffusivity at higher defect concentration, since at least one study<sup>18</sup> found that interstitial oxygen diffusivity in  $\text{CeO}_2$  increased beyond the dilute limit while vacancy oxygen diffusivity decreased. Fourth, oxygen surface exchange and catalytic reactions involving pulling oxygen to the surface are potentially faster when transport is mediated by interstitials as compared to vacancies, as the entire surface has accessible interstitial sites to absorb oxygen as interstitials. The synergistic combination of lower migration barriers, increasing concentration at low temperatures, and many active surface sites for exchange suggest that interstitial oxygen conductors may lead to large performance improvements in oxygen-active materials. Therefore, we propose that a promising path to expand the palette of highly oxygen-active materials at lower temperatures is to develop methods to discover and engineer interstitial oxygen conductors.

The imbalance in the number of known vacancy versus interstitial oxygen conductors is likely the result of the difficulty of forming interstitial oxygen in many materials, due to the large size of the oxygen anion. The oxides presently known to have predominantly interstitial-mediated oxygen conductivity remain constrained to seven families, including Ruddlesden-Popper<sup>19</sup>, apatite<sup>20</sup>, melillite<sup>21</sup>, mayenite,<sup>22</sup> scheelite<sup>23–25</sup>, hexagonal manganites<sup>26</sup>, and hexagonal perovskite<sup>27</sup>. Some of these systems (Ruddlesden-Popper  $\text{Nd}_2\text{NiO}_{4+\delta}$ ,<sup>28</sup> apatite  $\text{La}_{9.75}\text{Sr}_{0.25}\text{Si}_6\text{O}_{26.895}$ ,<sup>20</sup> melillite  $\text{La}_{1.54}\text{Sr}_{0.46}\text{Ga}_3\text{O}_{7.27}$ ,<sup>29</sup> scheelite  $\text{CeNbO}_{4+\delta}$ ,<sup>25</sup> and hexagonal perovskite  $\text{Ba}_7\text{Nb}_{3.9}\text{Mo}_{1.1}\text{O}_{20.05}$ )<sup>30</sup> were

reported to show high ionic conductivity, comparable to the commercial ionic conductor yttria-stabilized zirconia (YSZ). Despite this promising list, far less attention has been devoted to interstitial-dominated systems than vacancy-dominated ones, and an approach guided by fundamental understanding to discover new interstitial oxygen conductors is missing.

In this work, we proposed a practical approach based on structural and chemical features as well as *ab initio* calculations for finding high-performing interstitial oxygen conductors, identified multiple new promising structural classes, and demonstrated the exceptional performance of one example material,  $\text{La}_4\text{Mn}_5\text{Si}_4\text{O}_{22+\delta}$  (LMS) with experimental validation. These newly discovered material classes are distinct from any known oxygen ion conductors and would have been difficult to find given present understanding without such computational guidance. This study laid a foundation to dramatically increase the palette of interstitial oxygen conductors, enabling researchers to explore the advantages of interstitial oxygen conductors for the advancement of oxygen-active material applications.

### A descriptor approach for discovering new interstitial oxygen conductors

We proposed a set of simple descriptors (features) for discovering interstitial oxygen conductors based on material structure, composition, and readily available property data. The structure features are based on the hypothesis that (1) the facile formation of interstitial oxygen requires sufficient accessible volume and electrons from oxidizable transition metal cations, (2) the fast migration of interstitial oxygen should be enhanced by the presence of short diffusion pathways, a result consistent with intuition and the correlation between hop length and migration barrier found in oxygen vacancy diffusion within perovskites.<sup>31</sup> The property features are focused on thermodynamic stability and synthesizability. This led to screening on the following five structure and property features: (1) free space for interstitial

oxygen, (2) short hop distance, (3) thermodynamic stability, (4) oxidizability, and (5) synthesizability. It is important to acknowledge that there could be other features that enable the discovery of different or more materials. The proposed descriptors represent a logical first approach based on our current limited understanding of interstitial oxygen diffusers. One could quantify these features in different ways and here we use structures and properties from the Materials Project,<sup>32</sup> with the details given in **Methods 1**, step (1)-(5). We screened nearly 34k oxide materials with the five descriptors and retained 519 compounds, which were classified into 345 unique structural groups based on structural similarity analysis<sup>33</sup> (**Methods 1**, step (6)). One candidate for each group was selected for further validation with *ab initio* studies, discussed below. It is striking to note the power of these simple descriptors based on physical-intuition-guided hypotheses, as we quickly winnowed the field of 34k oxides down to 345, a 99% reduction in the search space enabled by basic analysis of material structure and composition.

### *Ab initio* computational screening of promising compounds for discovering new interstitial oxygen conductors

The above 6 screening steps based on structure, composition, and property data took only a couple of days on a fast processor. Then, we screened the resulting 345 compounds for promising cases by the formation energy ( $E_f$ ) and migration barriers ( $E_m$ ) of interstitial oxygen, calculated by the slower but more quantitative density functional theory (DFT) methods (“*ab initio* simulation” stage in **Fig. 2**). Specifically, compounds with  $E_f \leq 0.3$  eV (at  $P(\text{O}_2) = 0.2$  atm and  $T=300$  K) were considered promising (**Methods 2**, step (7)), and 80 out of the 345 compounds (23%) were retained (**Table S1**), suggesting that the use of simple descriptors in steps (1)-(6) was highly effective in winnowing the compound space to a tractable number of DFT calculations, while also retaining a considerable percentage of promising candidates. Next, *ab initio* molecular dynamics (AIMD) simulation was used to estimate  $E_m$  (**Methods 2**, step (8)). The AIMD calculations are

quite slow and as of this writing 26 out of the 80 compounds were studied and ranked by their estimated  $E_m$  (**Table S2**). 9 compounds with the estimated  $E_m \leq 0.86$  eV were selected for more accurate determination of  $E_m$  with long-time AIMD simulation. From these extended runs, 3 compounds with  $E_m \leq 0.5$  eV were identified as members of promising new families of interstitial oxygen conductors, which were  $\text{K}_2\text{Mn}_2(\text{MoO}_4)_3$ ,  $\text{La}_4\text{Mn}_5\text{Si}_4\text{O}_{22}$ , and  $\text{CeMn}_2\text{Ge}_4\text{O}_{12}$ . These three compounds are members of families of double molybdates  $\text{A}_2\text{TM}_2(\text{MoO}_4)_3$  (A=alkali metal, TM=transition metal),<sup>34</sup> perrierite/chevkinite  $\text{RE}_4\text{TM}_5\text{Si}_4\text{O}_{22}$  (RE=rare earth, TM=transition metal),<sup>35</sup> and germinates  $\text{RE}_1\text{TM}_2\text{Ge}_4\text{O}_{12}$  (RE= rare earth, TM=transition metal),<sup>36</sup> respectively.

These new families are a conservative estimate of the true number which could be uncovered with our present approach as many compounds have not yet been fully studied by AIMD and no effort was made to explore oxide structures not available in the Materials Project. More broadly, the approximate screening applied here may have introduced some compounds onto our lists that are not effective interstitial diffusers and conversely missed others that are. However, the success of this work in finding promising compounds—validated through *ab initio* methods and selected experiments—indicates that our screening process is sufficiently robust for discovering new materials, and we anticipate that finding compounds that might have been overlooked will be a focus for future work.  $\text{La}_4\text{Mn}_5\text{Si}_4\text{O}_{22}$  (LMS) was selected as a representative member of the perrierite/chevkinite family for experimental investigation due to its predicted fast interstitial oxygen diffusion, simple established synthesis method,<sup>37</sup> and inclusion of inexpensive, readily available, and non-toxic elements, which are all traits desirable for new oxygen-active materials potentially useful in a variety of applications.

## Understanding universal features of high-performing interstitial oxygen conductors

Here we uncover the universal features that enable certain material structures to be highly effective interstitial oxygen formers and conductors. Specifically, we examined the three newly discovered structural families in this study and all of the previously known high-performing interstitial oxygen conductors of which we are aware—apatite,<sup>1</sup> melilite,<sup>2</sup> scheelite,<sup>3</sup> mayenite,<sup>4</sup> Ruddlesden-Popper,<sup>5</sup> hexagonal perovskite,<sup>6,7</sup> and hexagonal manganites<sup>8</sup> (all displayed in **Fig. 3**). Other materials have demonstrated some degree of interstitial oxygen diffusion, e.g., fluorite,<sup>9</sup> corundum,<sup>10</sup> silica,<sup>11</sup> garnet,<sup>12</sup> cuspidine,<sup>13</sup> and langasite<sup>14</sup>. However, these materials are excluded for our considerations as we believe the existing examples are poor oxygen conductors based on their having high oxygen interstitial formation energy<sup>11</sup> or migration barrier,<sup>9,13,14</sup> or the material having known extremely low ionic conductivity.<sup>12</sup> Through detailed inspection of both the newly discovered and the previously known high-performing interstitial oxygen conductors, we have identified the following electronic and atomic structure features that are crucial for effectively incorporating and diffusing interstitial oxygen: (i) the availability of electrons for oxygen reduction and (ii) structural flexibility enabling sufficient accessible volume. Within the ten families we have identified, the availability of electrons is accomplished through the presence of oxidizable cations or aliovalent doping with electron donors (i.e., donor cation substitution). The structural flexibility is associated with one of two structural motifs: (i) corner-sharing polyhedral networks or (ii) isolated polyhedra. These two types of flexible polyhedral networks can both accommodate excess interstitial oxygen and enable their mobility through easy deformation, leading to low formation and migration barriers for interstitial oxygen. Notably, the corner-sharing polyhedral network is also a structural characteristic often recognized as advantageous in fast Li-ion conduction,<sup>38,39</sup> suggesting a broader applicability of the structural flexibility feature. The revelation of these two essential features across the high-

performing families has significantly advanced our knowledge of interstitial oxygen conductors, and provides a new framework for discovering and optimizing materials in this domain. More details about the origin of available electrons and how the two structural motifs facilitate interstitial oxygen diffusion are given in **SI Discussion 2**.

## Structure of $\text{La}_4\text{Mn}_5\text{Si}_4\text{O}_{22+\delta}$

LMS was first reported by Gueho *et al.* with structure and magnetic data in 1995,<sup>37</sup> with no further studies of which we are aware. LMS is a layered sorosilicate material with multivalent manganese and isostructural with perrierite and chevkinite, which crystallizes in the space group  $C2/m$ . In **Fig. 4a**, LMS displays eclipsed sorosilicate  $\text{Si}_2\text{O}_7$  groups separated by rutile-like sheets of edge-shared  $\text{Mn}_1^{4+}/\text{Mn}_2^{3+}$  octahedra and single isolated  $\text{Mn}_3^{2+}$  octahedra. The stoichiometric primitive cell has two  $\text{Mn}_1^{4+}$ , two  $\text{Mn}_2^{3+}$ , and one  $\text{Mn}_3^{2+}$ , where their valence states assignment fully consistent with the magnetic moments observed in the DFT calculations (**SI Discussion 5**). Sorosilicate  $\text{Si}_2\text{O}_7$  groups show a zigzag arrangement along the a-axis, connect with  $\text{Mn}_3^{2+}$  octahedra along b-axis and  $\text{Mn}_2^{3+}$  octahedra along c-axis by sharing corners, leaving free space in between these unconnected  $\text{Si}_2\text{O}_7$  chains. The La atoms are between the rutile-like layer and the sorosilicate layer, surrounded by 10 oxygen atoms. The structure has ample free space, a highly flexible network, and multiple Mn ions potentially capable of oxidation, making it ideally suited to form and transport interstitial oxygen.

## A dual diffusion mechanism enabled by unconnected sorosilicate groups and flexible corner-sharing framework

We note that all *ab initio* studies for LMS in this study were performed using the strongly constrained and appropriately normed (SCAN) functional,<sup>40</sup> as it outperformed other functionals in predicting all available experimental data such as lattice parameters, optical band gap, interstitial oxygen concentration and diffusion barrier acquired in this study (Details provided in **SI**

**Discussion 3).** *Ab initio* studies and simple thermodynamic considerations suggest that excess oxygen with  $\text{La}_4\text{Mn}_5\text{Si}_4\text{O}_{22+\delta}$  ( $\delta \approx 0.5$ ) is thermodynamically favorable under air conditions, while oxygen vacancies are very unfavorable due to their high formation energy (**SI Discussion 4**). In **Fig. 4a**, the most stable interstitial site ( $O_i^1$ ) lies in between two adjacent sorosilicate  $\text{Si}_2\text{O}_7$  groups, connecting two Si tetrahedra, and the second most stable interstitial site ( $O_i^2$ ) lies in the joint of the  $\text{Si}_2\text{O}_7$  and the  $\text{Mn}_3^{2+}$  octahedra. These two prevailing interstitial sites contribute two distinct and competitive diffusion pathways. In the interstitial diffusion mechanism (yellow arrow in **Fig. 4a**), the  $O_i$  hops between the  $O_i^1$  sites through the channel between sorosilicate chains along the a-axis. A parallel active interstitialcy (cooperative “knock-on”) mechanism is indicated by cyan arrows, in which the  $O_i$  moves along the corner-sharing  $\text{Si}_2\text{O}_7$ - $\text{MnO}_2$ - $\text{Si}_2\text{O}_7$  framework along the b-axis. In the interstitialcy mechanism, the  $O_i$  first hops from the  $O_i^1$  site to a lattice site by kicking a lattice oxygen to the  $O_i^2$  site, which then moves to a lattice site by kicking another lattice oxygen to the next  $O_i^1$  site. The energy landscape along the diffusion pathways reveals migration barriers of 0.69 eV and 0.74 eV for the interstitial and interstitialcy mechanisms, respectively, calculated by Climbing Image Nudged Elastic Band (CI-NEB) method (**Fig. S2a**). These values are in excellent agreement with the experimentally determined activation energy of 0.78 eV discussed below. Both pathways contribute to the diffusion, supported by their simultaneous occurrences AIMD simulations (**Movie S1**) and the small energetic difference (0.05 eV) in migration barriers for both mechanisms. To confirm the prevalence of these two diffusion mechanisms across a broad temperature range, extensive molecular dynamics simulations were conducted by AIMD using generalized gradient approximation exchange-correlation functional of Perdew, Burke, and Ernzerhof (GGA-PBE)<sup>41</sup> and machine learning-trained interatomic potential molecular dynamics (ML-IPMD) simulations (**Methods 3-4**) (we did not use SCAN for long-time AIMD simulation due to its high computational cost). The oxygen tracer diffusion coefficient achieved from GGA-PBE AIMD and ML-IPMD

consistently confirms to the Arrhenius fitting over a wide temperature range (**Fig. S3**). The AIMD migration barrier shows excellent agreement with the ML-IPMD results, as well as the GGA-PBE CI-NEB barriers in **Fig. S2b**. These results demonstrate the dual diffusion mechanism dominates the oxygen ion diffusion at both high and low temperatures. The DFT predictions of stable interstitials with low migration barriers indicate that  $\text{La}_4\text{Mn}_5\text{Si}_4\text{O}_{22+\delta}$  is a fast oxygen conductor.

Nearly all known interstitial oxygen conductors diffuse oxygen ions through an interstitialcy mechanism. The prevalence of the interstitialcy mechanism is likely due to the large size of the oxygen anion and the lack of available diffusion channels. A pure interstitial diffusion mechanism through channels is rare, and, to our knowledge, only found in apatites and scheelite, which both feature isolated polyhedra. LMS adopts a dual-diffusion mechanism, where the oxygen diffusion consists of both interstitial and interstitialcy pathways. The pure interstitial diffusion channel between the unconnected sorosilicate chains has a slightly lower energy barrier than the interstitialcy pathway, with a difference of 0.05 eV according to the SCAN CI-NEB calculations. The interstitial diffusion occurs due to the free space between the zigzag-arranged unconnected sorosilicate chains and the adjacent  $\text{Mn}_3^{2+}$  ion, which create a stable channel for the interstitial oxygen. The interstitialcy diffusion happens through the rotation of the corner-sharing framework  $\text{Si}_2\text{O}_7$ - $\text{MnO}_2$ - $\text{Si}_2\text{O}_7$ , which help stabilize the interstitial oxygen and facilitate diffusion. This dual mechanism is distinct from any confirmed mechanisms for an interstitial oxygen conductor of which we are aware.

### Experimental confirmation of interstitial oxygen conductor $\text{La}_4\text{Mn}_5\text{Si}_4\text{O}_{22+\delta}$

To validate the computational predictions, we synthesized LMS and studied its oxygen concentration, conductivity, and oxygen surface exchange rate. A molten salt synthesis method was used (**Methods 5**). The monoclinic perrierite (C2/m) structure of LMS was confirmed by Rietveld-

refinement of room temperature X-ray diffraction (XRD) data (**Fig. 4b**), and the consistency of the obtained lattice parameters with previous literature values (**Table S4**). LMS pellets were sintered at 1050 °C for 24h for the elemental and electrical characterizations. The field emission scanning electron microscope (FESEM) image of sintered LMS pellet (**Fig. S5**) confirmed its high density with minimal porosity through the sample. The composition was determined as  $\text{La}_{4.00}\text{Mn}_{4.69}\text{Si}_{4.03}\text{O}_{22.42}$  by electron probe micro-analyzer (EPMA) analysis, suggesting significant Mn deficiency, small Si excess, and significant excess oxygen with  $\delta = 0.42$ . Interstitial oxygen was also verified by the iodometric titration method with  $\delta = 0.47$  (**Table S6, SI Discussion 6**). X-ray photoemission spectroscopy (XPS) analysis qualitatively supported the presence of interstitial oxygen (**Fig. 4c**). Deconvolution of the core level O1s spectra reveals three peaks. The peaks at 530.4 eV and 532.1 eV are associated with the lattice oxygen<sup>42,43</sup> and surface chemisorbed oxygen,<sup>44</sup> respectively. The low binding energy peak at 528.9 eV represents the interstitial oxygen within LMS.<sup>42</sup> The XPS survey scan on the LMS pellet surface revealed the presence of La, Mn, Si, and O without any detectable impurity elements (**Fig. S6**). Thermogravimetric analysis (TGA) was performed to study the temperature dependence of oxygen content (**Methods 8, Fig. S7**). Almost no change of the total mass was observed when heating/cooling the LMS powder, which aligns with the *ab initio* studies on the interstitial oxygen concentration in **SI Discussion 4**. These results suggest that the interstitial oxygen is charge balanced by oxidizing  $\text{Mn}^{2+}$  ions and its concentration is highly constrained by the concentration of  $\text{Mn}^{2+}$  ions, corresponding to  $\delta = 0.5$  when all the  $\text{Mn}^{2+}$  ions are oxidized.

LMS is a semiconductor with a narrow indirect band gap of 0.79 eV measured by UV-vis spectroscopy (**Fig. S8**), indicating that LMS could have electron conduction at high temperatures due to thermal excitation. The band gap calculated by *ab initio* method with SCAN functional is 0.72 eV, consistent with experiment (**Table S3, SI Discussion 3**). The 4-probe conductivity measurement shows

that LMS is a mixed ionic-electronic conductor (**Fig. S9**). Ionic conductivity ( $\sigma_{ion}$ ) of LMS was measured using electron blocking 8YSZ,<sup>45</sup> and our setup was verified by obtaining robust results on the well-studied mixed conductor  $\text{La}_{0.6}\text{Sr}_{0.4}\text{Co}_{0.2}\text{Fe}_{0.8}\text{O}_3$  (LSCF) (**Methods 9 and Fig. S10-11**). In **Fig. 4d**, LMS has comparable ionic conductivity to many of the best fast oxygen conductors and considerably higher ionic conductivity than widely used commercial materials such as LSCF and YSZ. In addition, LMS has comparable or improved ionic conductivity compared to other interstitial oxygen conductors, such as hexagonal perovskite  $\text{Ba}_7\text{Nb}_{3.9}\text{Mo}_{1.1}\text{O}_{20.05}$ , apatite  $\text{La}_{9.75}\text{Sr}_{0.25}\text{Si}_6\text{O}_{26.895}$ , Ruddlesden-Popper  $\text{Nd}_2\text{NiO}_{4+\delta}$ , scheelite  $\text{CeNbO}_{4+\delta}$ , and melilite  $\text{La}_{1.54}\text{Sr}_{0.46}\text{Ga}_3\text{O}_{7.27}$ . The experimental activation barrier of oxygen ion conduction in LMS is  $0.78 \pm 0.07$  eV, determined by the Arrhenius relation  $\sigma T = \sigma_0 e^{\left(\frac{-E_A}{k_b T}\right)}$  (**Methods 11**). Given there is almost no temperature dependence of oxygen stoichiometry from TGA, this experimental  $E_A$  is expected to be similar to the DFT SCAN CI-NEB calculated migration barriers  $E_m$ , which are 0.69 eV and 0.74 eV for interstitial and interstitialcy diffusion, respectively. The excellent agreement between the experimental and DFT predicted energy barriers further supports the correctness of DFT modeling, which in turn supports the dual diffusion mechanism for oxygen diffusion in LMS. In **Fig. 4d**, the inserted figure displays a comparison of ionic conductivity derived from *ab initio* studies (**SI Discussion 11**) with experimental data. The DFT conductivity exhibits a remarkably consistent trend and slightly higher values compared to experiments. The minor difference may come from many factors, e.g., sample impurities, grain boundary effects, and both DFT and experimental limitations.

To further probe the oxygen kinetics in LMS, the oxygen surface exchange coefficient ( $k_{chem}$ ) and the chemical oxygen diffusivity ( $D_{chem}$ ) were studied using the electrical conductivity relaxation (ECR) method. The Arrhenius plots of  $D_{chem}$  and  $k_{chem}$  of LMS in **Fig. 4e** show that LMS has  $D_{chem}$  and  $k_{chem}$  comparable to numerous state-of-art solid oxide electrode materials over a

wide range of temperatures. LMS has among the highest  $k_{chem}$  values at low temperatures of any known material, in part due to the relatively small activation energy of 0.82 eV for oxygen surface exchange (**Methods 11**). The enhanced  $k_{chem}$  of LMS at low temperatures compared to vacancy-mediated diffusers might be due to there being more surface interstitial sites than vacancy sites available for oxygen exchange, but further study is needed to understand the interstitial surface exchange mechanism.

## Discussion

The experimental tracer diffusion coefficient ( $D^*$ ) was determined using the Nernst-Einstein equation, the experimental  $\sigma_{ion}$  and  $\delta$ , and the *ab initio*-derived Haven ratio (**Methods 11**). The thermodynamic factor  $\gamma$  and the tracer surface exchange coefficient ( $k^*$ ) were evaluated by  $D_{chem} = \gamma D^*$  and  $k_{chem} = \gamma k^*$ .<sup>46</sup> The thermodynamic factor of LMS varies from 13.6 to 17.7 in the temperature range of 600 to 750 °C (**Fig. S13f**), which is about 15 to 30 times smaller than that of the commonly studied mixed ionic electronic conducting perovskites LSCF,<sup>47</sup> BCFZr,<sup>48</sup> and BSCF.<sup>49</sup> The small  $\gamma$  and high  $k_{chem}$  imply LMS will have high  $k^*$  compared with other state-of-the-art materials. **Fig. S15** shows that LMS has a higher  $k^*$  at intermediate and low temperatures than state-of-the-art materials, perhaps even exceeding that of the leading BSCF material. The high surface exchange rate suggests LMS has the potential to assist in achieving fast oxygen reduction kinetics, e.g., reducing area specific resistance in the air electrode of solid oxide cells for electricity or hydrogen production, although its low electronic conductivity means it would have to be used as a composite with a good electrical conductor in many applications.<sup>50</sup>

This work demonstrates the largely untapped potential of interstitial oxygen ion conductors for reduced temperature oxygen-active material applications. We have designed a simple but effective method using physically-motivated descriptors and *ab initio* calculations to search for new families of interstitial oxygen diffusers. The

effectiveness of our approach was confirmed by prediction and experimental confirmation of an entirely new class of predominantly interstitial oxygen conductor, represented by  $\text{La}_4\text{Mn}_5\text{Si}_4\text{O}_{22+\delta}$  (LMS). LMS has very fast oxygen surface exchange and transport through both interstitial and interstitialcy mechanisms, which are enabled by the free space between unconnected sorosilicate chains, corner-sharing framework  $\text{Si}_2\text{O}_7$ - $\text{MnO}_2$ - $\text{Si}_2\text{O}_7$ , and high redox activity of the nearby  $\text{Mn}_3^{2+}$  ion. We note that LMS is just one example of the broader perrierite/chevkinite  $\text{RE}_4\text{TM}_5\text{Si}_4\text{O}_{22}$  structural family, other compositions within this family or composition and/or microstructure refinement of LMS itself may yield additional materials with fast oxygen interstitial transport. We also proposed that families of double molybdates  $\text{A}_2\text{TM}_2(\text{MoO}_4)_3$  and germinates  $\text{RE}_1\text{TM}_2\text{Ge}_4\text{O}_{12}$  are promising for further study.

The success of our approach suggests that we have identified relatively simple structural and chemical features that strongly correlate with stable interstitial oxygen formation and fast migration. The universal features of all newly discovered and previously known interstitial oxygen conductors include: (i) the availability of electrons for oxygen reduction and (ii) structural flexibility enabling sufficient accessible volume. We speculate that these are two essential features to effectively incorporate and diffuse interstitial oxygen. The structural flexibility is associated with structural motifs of either corner-sharing polyhedral networks or isolated polyhedra. These findings provide new insights into interstitial oxygen conductors and guidance for their discovery, including strategies like targeted cation substitution in materials with these specific structural motifs, as well as exploration of alternative structural motifs featuring high structural flexibility.

## Reference

1. Wachsman, E. D. & Lee, K. T. Lowering the temperature of solid oxide fuel cells. *Science* **334**, 935–939 (2011).

2. Jacobson, A. J. Materials for Solid Oxide Fuel Cells. *Chem. Mater.* **22**, 660–674 (2010).
3. Vøllestad, E. *et al.* Mixed proton and electron conducting double perovskite anodes for stable and efficient tubular proton ceramic electrolyzers. *Nat. Mater.* **18**, 752–759 (2019).
4. Choi, S. *et al.* Exceptional power density and stability at intermediate temperatures in protonic ceramic fuel cells. *Nat. Energy* **3**, 202–210 (2018).
5. Duan, C. *et al.* Highly efficient reversible protonic ceramic electrochemical cells for power generation and fuel production. *Nat. Energy* **4**, 230–240 (2019).
6. Hong, W. T., Risch, M., Stoerzinger, K. A. & Grimaud, A. Toward the rational design of non-precious transition metal oxides for oxygen electrocatalysis. *Energy Environ. Sci.* **8**, 1404–1427 (2015).
7. Zhang, C. & Huang, K. Solid-oxide metal–air redox batteries. In *Solid Oxide-Based Electrochemical Devices* 217–250 (Elsevier, 2020).
8. Eranna, G., Joshi, B. C., Runthala, D. P. & Gupta, R. P. Oxide Materials for Development of Integrated Gas Sensors—A Comprehensive Review. *Critical Reviews in Solid State and Materials Sciences* **29**, 111–188 (2004).
9. Hossain, M. M. & Lasa, H. I. de. Chemical-looping combustion (CLC) for inherent CO<sub>2</sub> separations—a review. *Chem. Eng. Sci.* **63**, 4433–4451 (2008).
10. Yang, J. J., Strukov, D. B. & Stewart, D. R. Memristive devices for computing. *Nat. Nanotechnol.* **8**, 13–24 (2013).
11. Petric, A., Huang, P. & Tietz, F. Evaluation of La–Sr–Co–Fe–O perovskites for solid oxide fuel cells and gas separation membranes. *Solid State Ion.* **135**, 719–725 (2000).
12. Funke, K. Solid State Ionics: from Michael Faraday to green energy—the European dimension. *Sci. Technol. Adv. Mater.* **14**, 43502 (2013).
13. van Gool, W. Fast ion conduction. *Annu. Rev. Mater. Sci.* **4**, 311–335 (1974).
14. Heider, U., Jörissen, L., Huggins, R. A. & Witschel, W. Oxygen ion conductivity in doped Gd<sub>2</sub>Ti<sub>2</sub>O<sub>7</sub> with the pyrochlore structure. *Ionic* **2**, 7–11 (1996).
15. Huang, K., Tichy, R. S. & Goodenough, J. B. Superior Perovskite Oxide-Ion Conductor; Strontium- and Magnesium-Doped LaGaO<sub>3</sub>: I, Phase Relationships and Electrical Properties. *J. Am. Ceram. Soc.* **75**, 2565 (1998).
16. Skinner, S. J. & Kilner, J. A. Oxygen Ion Conductors. *Mater. Today* **6**, 30–37 (2003).
17. Antono, E., Meredig, B., & Mulholland, G. J. Citrine Informatics ARPA-E Ionics Database. <https://citrination.com/datasets/151085> (accessed August 18).
18. Waldow, S. P., & De Souza, R. A. Is excess faster than deficient? A molecular- dynamics study of oxygen-interstitial and oxygen- vacancy diffusion in CeO<sub>2</sub>. *J. Phys. Energy* **2** 024001 (2020).
19. Xu, S., Jacobs, R. & Morgan, D. Factors Controlling Oxygen Interstitial Diffusion in the Ruddlesden–Popper Oxide La<sub>2–x</sub>Sr<sub>x</sub>NiO<sub>4+δ</sub>. *Chem. Mater.* **30**, 7166–7177 (2018).
20. Arikawa, H., Nishiguchi, H., Ishihara, T. & Takita, Y. Oxide ion conductivity in Sr-doped La<sub>10</sub>Ge<sub>6</sub>O<sub>27</sub> apatite oxide. *Solid State Ion.* **136–137**, 31–37 (2000).
21. Schuett, J., Schultze, T. K. & Grieshammer, S. Oxygen Ion Migration and Conductivity in LaSrGa<sub>3</sub>O<sub>7</sub> Melilites from First Principles. *Chem. Mater.* **32**, 4442–4450 (2020).
22. Lacerda M. *et al.* High oxide ion conductivity in Ca<sub>12</sub>Al<sub>14</sub>O<sub>33</sub>. *Nature* **332**, 525–526 (1988).
23. Li, J. *et al.* Modulated structure determination and ion transport mechanism of oxide-ion conductor CeNbO<sub>4+δ</sub>. *Nat. Commun.* **11**, 1–9 (2020).
24. Pramana, S. S. *et al.* Correlation of Local Structure and Diffusion Pathways in the Modulated Anisotropic Oxide Ion Conductor CeNbO<sub>4.25</sub>. *J. Am. Chem. Soc.* **138**, 1273–1279 (2016).
25. Packer, R. J. *et al.* Lanthanum substituted CeNbO<sub>4+δ</sub> scheelites: Mixed conductivity and structure at elevated temperatures. *J. Mater. Chem.* **16**, 3503–3511 (2006).
26. Skjærvø, S. H. *et al.* Interstitial oxygen as a source of p-type conductivity in hexagonal manganites. *Nat. Commun.* **7**, 7491 (2016).
27. Yashima, M. *et al.* High oxide-ion conductivity through the interstitial oxygen site in Ba<sub>7</sub>Nb<sub>4</sub>MoO<sub>20</sub>-based hexagonal perovskite related oxides. *Nat. Commun.* **12**, 1–7 (2021).
28. Song, J., Ning, D., Boukamp, B., Bassat, J. M. & Bouwmeester, H. J. M. Structure, electrical conductivity and oxygen transport properties of Ruddlesden-Popper phases Ln<sub>n+1</sub>Ni<sub>n</sub>O<sub>3n+1</sub> (Ln = La, Pr and Nd; n = 1, 2 and 3). *J. Mater. Chem. A* **8**, 22206–22221 (2020).

29. Thomas, C. I. *et al.* Phase stability control of interstitial oxide ion conductivity in the  $\text{La}_{1-x}\text{Sr}_x\text{Ga}_3\text{O}_{7+x/2}$  Melilite Family. *Chem. Mater.* **22**, 2510–2516 (2010).
30. Fop, S. *et al.* High oxide ion and proton conductivity in a disordered hexagonal perovskite. *Nat. Mater.* **19**, 752–757 (2020).
31. Mayeshiba, T. T. & Morgan, D. D. Factors controlling oxygen migration barriers in perovskites. *Solid State Ion.* **296**, 71–77 (2016).
32. Jain, A. *et al.* Commentary: The Materials Project: A materials genome approach to accelerating materials innovation. *APL Mater.* **1**, 11002 (2013).
33. Pan, H. *et al.* Benchmarking Coordination Number Prediction Algorithms on Inorganic Crystal Structures. *Inorg. Chem.* **60**, 1590–1603 (2021).
34. Solodovnikov, S. F., Klevtsova, R. F., Kim, V. G. & Klevtsov, P. V. Double molybdates of composition  $\text{CsR}_2^{2+}(\text{MoO}_4)_3$  (R=Ni, Co, Mg, Mn, Cd) and the crystal structure of  $\text{Cs}_2\text{Co}_2(\text{MoO}_4)_3$ . *J. Struct. Chem.* **27**, 928–933 (1986).
35. Ito, Jun; Arem, J. E. Checkinite and perrierite: synthesis, crystal growth and polymorphism. *Am. Mineral.* **56**, 307–319 (1971).
36. Taviot-Guého, C., Léone, P., Palvadeau, P. & Rouxel, J.  $\text{CeMn}_2\text{Ge}_4\text{O}_{12}$ -Synthesis and Structural Characterization of Two New Rare-Earth Manganese Germanates:  $\text{CeMn}_2\text{Ge}_4\text{O}_{12}$  and  $\text{GdMnGe}_2\text{O}_7$ . *J. Solid State Chem.* **143**, 145–150 (1999).
37. Gueho, C., Giaquinta, D., Mansot, J. L., Ebel, T. & Palvadeau, P. Structure and Magnetism of  $\text{La}_4\text{Mn}_5\text{Si}_4\text{O}_{22}$  and  $\text{La}_4\text{V}_5\text{Si}_4\text{O}_{22}$ : Two New Rare-Earth Transition Metal Sorosilicates. *Chem. Mater.* **7**, 486–492 (1995).
38. Jun, K. J. *et al.* Lithium superionic conductors with corner-sharing frameworks. *Nat. Mater.* **21**, 924–931. (2022).
39. Muy, S., Schlem, R., Shao-Horn, Y. & Zeier, W. G. Phonon–Ion Interactions: Designing Ion Mobility Based on Lattice Dynamics. *Adv. Energy Mater.* **11**, 1–14 (2021).
40. Sun, J., Ruzsinszky, A. & Perdew, J. Strongly Constrained and Appropriately Normed Semilocal Density Functional. *Phys. Rev. Lett.* **115**, 1–6 (2015).
41. Perdew, J., Burke, K. & Ernzerhof, M. Generalized Gradient Approximation Made Simple. *Phys. Rev. Lett.* **77**, 3865–3868 (1996).
42. Kumar, U., Yadav, D. & Upadhyay, S. Investigation of structural, optical, and magnetic properties of Nd-doped  $\text{Sr}_2\text{SnO}_4$  Ruddlesden Popper oxide. *J. Am. Ceram. Soc.* **103**, 5743–5757 (2020).
43. Kumar, U. & Upadhyay, S. Investigation of structural, optical and electrical properties of  $\text{Sr}_2\text{SnO}_4$ ,  $\text{Sr}_{1.99}\text{Eu}_{0.01}\text{SnO}_4$  and  $\text{Sr}_2\text{Sn}_{0.99}\text{Eu}_{0.01}\text{O}_4$  Ruddlesden Popper oxide. *Mater. Res. Express* **6**, 55805 (2019).
44. Islam, M. N., Ghosh, T. B., Chopra, K. L. & Acharya, H. N. XPS and X-ray diffraction studies of aluminum-doped zinc oxide transparent conducting films. *Thin Solid Films* **280**, 20–25 (1996).
45. Lei, C., Simpson, M. F. & Virkar, A. V. Investigation of Ion and Electron Conduction in the Mixed Ionic-Electronic Conductor- La-Sr-Co-Fe-Oxide (LSCF) Using Alternating Current (AC) and Direct Current (DC) Techniques. *J. Electrochem. Soc.* **169**, 014506 (2022).
46. Du, Yong, *et al.* Fundamentals of Thermophysical Properties. In *Computational Design of Engineering Materials: Fundamentals and Case Studies*. Cambridge University Press, 2023.
47. Endler-Schuck, C., Joos, J., Niedrig, C., Weber, A. & Ivers-Tiffée, E. The chemical oxygen surface exchange and bulk diffusion coefficient determined by impedance spectroscopy of porous  $\text{La}_{0.58}\text{Sr}_{0.4}\text{Co}_{0.2}\text{Fe}_{0.8}\text{O}_{3-\delta}$  (LSCF) cathodes. *Solid State Ion.* **269**, 67–79 (2015).
48. Zohourian, R., Merkle, R. & Maier, J. Proton uptake into the protonic cathode material  $\text{BaCo}_{0.4}\text{Fe}_{0.4}\text{Zr}_{0.2}\text{O}_{3-\delta}$  and comparison to protonic electrolyte materials. *Solid State Ion.* **299**, 64–69 (2017).
49. Bucher, E., Egger, A., Ried, P., Sitte, W. & Holtappels, P. Oxygen nonstoichiometry and exchange kinetics of  $\text{Ba}_{0.5}\text{Sr}_{0.5}\text{Co}_{0.8}\text{Fe}_{0.2}\text{O}_{3-\delta}$ . *Solid State Ion.* **179**, 1032–1035 (2008).
50. Jacobs, R. *et al.* Unconventional Highly Active and Stable Oxygen Reduction Catalysts Informed by Computational Design Strategies. *Adv. Energy Mater.* **12**, 2201203 (2022).
51. D. W. Strickler and W. G. Carlson. Electrical Conductivity in the  $\text{ZrO}_2$ -Rich Region of Several  $\text{M}_2\text{O}_3$ - $\text{ZrO}_2$  Systems. *J. Am. Ceram. Soc.* **48**, 286–289 (1965).
52. Steele, B. C. H. Appraisal of  $\text{Ce}_{1-y}\text{Gd}_y\text{O}_{2-y/2}$  electrolytes for IT-SOFC operation at 500 °C. *Solid State Ion.* **129**, 95–110 (2000).
53. Bucher, E., Egger, A., Ried, P., Sitte, W. & Holtappels, P. Oxygen nonstoichiometry and

exchange kinetics of  $\text{Ba}_{0.5}\text{Sr}_{0.5}\text{Co}_{0.8}\text{Fe}_{0.2}\text{O}_{3-\delta}$ .  
*Solid State Ion.* **179**, 1032–1035 (2008).

54. Li, M. *et al.* A family of oxide ion conductors based on the ferroelectric perovskite  $\text{Na}_{0.5}\text{Bi}_{0.5}\text{TiO}_3$ . *Nat. Mater.* **13**, 31–35 (2014).

## Figures

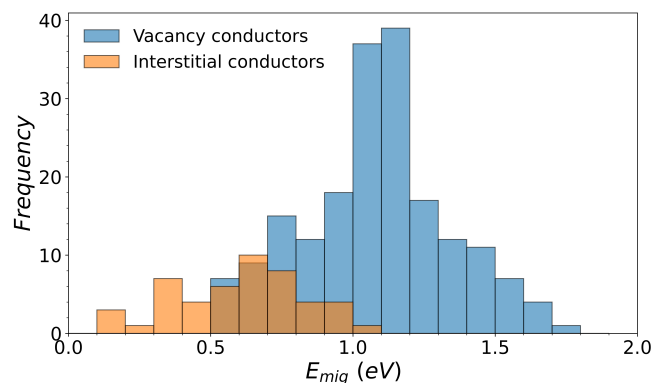


**Figure 1.** Migration barrier comparison of known interstitial and vacancy diffuser oxides obtained from the Citrine Informatics database<sup>17</sup> and literature. Data is available in digital Supplementary files.

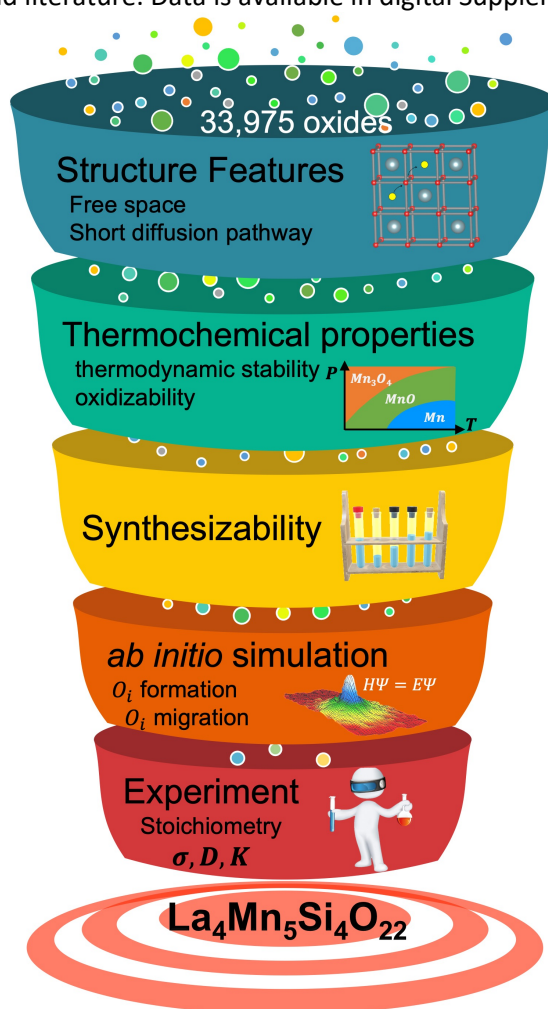


**Figure 2.** Schematic diagram of the screening approach for new interstitial oxygen conductors.

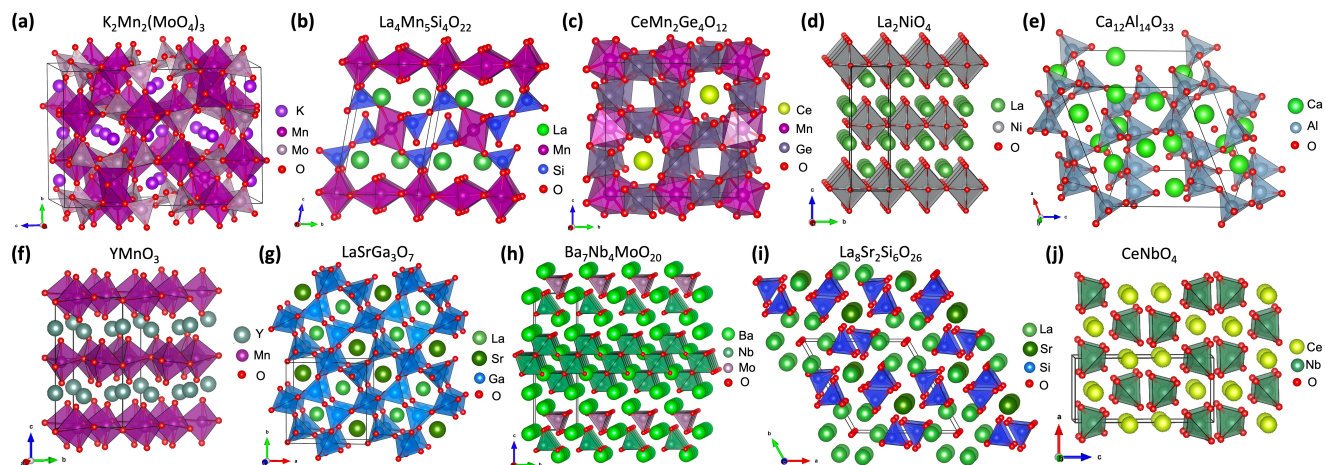


**Figure 3.** Bulk structure of fast interstitial oxygen conductors. (a)  $K_2Mn_2(MoO_4)_3$  (double molybdates  $A_2TM_2(MoO_4)_3$  ( $A$ =alkali metal,  $TM$ =transition metal) family), (b)  $La_4Mn_5Si_4O_{22}$  (perrierite/chevkinite  $RE_4TM_5Si_4O_{22}$  ( $RE$ =rare earth,  $TM$ =transition metal) family), (c)  $CeMn_2Ge_4O_{12}$  (germinates  $RE_1TM_2Ge_4O_{12}$  ( $RE$ = rare earth,  $TM$ =transition metal) family), (d)  $La_2NiO_4$  (Ruddlesden-Popper perovskite family), (e)  $Ca_{12}Al_{14}O_{33}$  (mayenite cage-compound family), (f)  $YMnO_3$  (hexagonal manganite family), (g)  $SrLa_4Ga_3O_7$  (melilite family), (h)  $Ba_7Nb_4MoO_{20}$  (hexagonal perovskite family), (i)  $La_8Sr_2Si_6O_{26}$  (apatite family), (j)  $CeNbO_4$  (scheelite family).

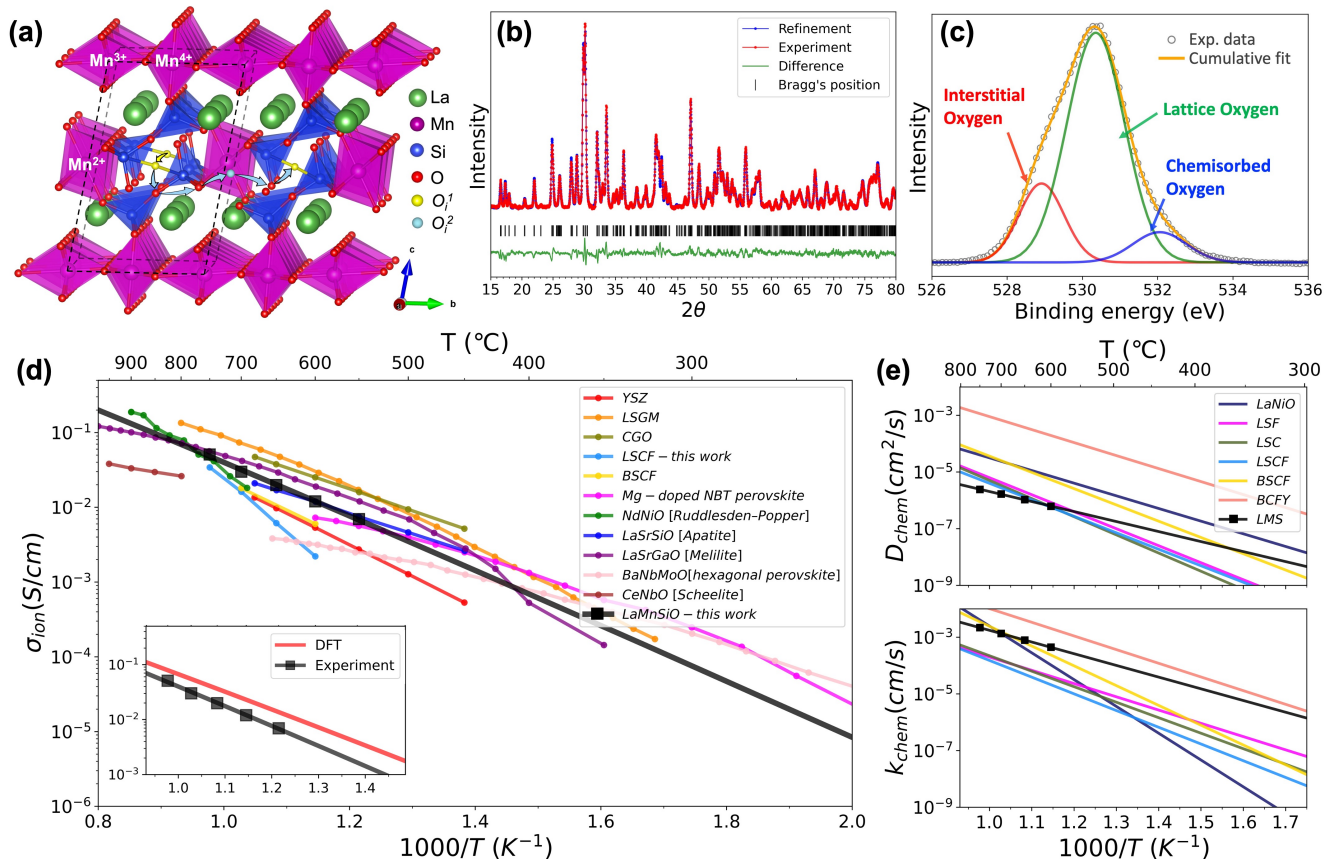


**Figure 4.** (a) Bulk structure of the  $\text{La}_4\text{Mn}_5\text{Si}_4\text{O}_{22}$ . The La, Mn, Si, and O sites are shown as green, purple, blue, and red spheres, respectively. The black dash line denotes the single unit cell. The yellow ball represents the  $\text{O}_1^i$  site and the cyan ball represents the  $\text{O}_2^i$  site, respectively. Interstitial Oxygen ( $\text{O}_i$ ) in LMS diffuses through both interstitial mechanism (yellow arrow) and interstitialcy (cooperative “knock-on”) mechanism (cyan arrows). (b) Room temperature X-ray diffraction pattern of  $\text{La}_4\text{Mn}_5\text{Si}_4\text{O}_{22+\delta}$  (LMS) and corresponding Rietveld refinement. (c) The peak-fitting results of  $\text{O}1s$  XPS spectra. (d) Arrhenius plots of the measured ionic conductivity of LMS compared with the leading oxygen ion conductors  $\text{Zr}_{0.92}\text{Y}_{0.08}\text{O}_{2-\delta}$  [YSZ],<sup>51</sup>  $\text{La}_{0.8}\text{Sr}_{0.2}\text{Ga}_{0.83}\text{Mg}_{0.17}\text{O}_{3-\delta}$  [LSGM],<sup>15</sup>  $\text{Ce}_{0.9}\text{Gd}_{0.1}\text{O}_{1.95}$  [CGO],<sup>52</sup>  $(\text{La}_{0.6}\text{Sr}_{0.4})_{0.95}\text{Co}_{0.2}\text{Fe}_{0.8}\text{O}_{3-\delta}$  [LSCF - this work],  $\text{Ba}_{0.5}\text{Sr}_{0.5}\text{Co}_{0.8}\text{Fe}_{0.2}\text{O}_{3-\delta}$  [BSCF],<sup>53</sup>  $\text{Na}_{0.5}\text{Bi}_{0.49}\text{Ti}_{0.98}\text{Mg}_{0.02}\text{O}_{2.965}$  [Mg-doped NBT perovskite],<sup>54</sup>  $\text{Nd}_2\text{NiO}_{4+\delta}$  [Ruddlesden-Popper],<sup>28</sup>  $\text{La}_{9.75}\text{Sr}_{0.25}\text{Si}_6\text{O}_{26.895}$  [Apatite],<sup>20</sup>  $\text{La}_{1.54}\text{Sr}_{0.46}\text{Ga}_3\text{O}_{7.27}$  [Melilite],<sup>29</sup>  $\text{Ba}_7\text{Nb}_{3.9}\text{Mo}_{1.1}\text{O}_{20.05}$  [hexagonal perovskite],<sup>30</sup> and  $\text{CeNbO}_{4+\delta}$  [Scheelite].<sup>25</sup> Inserted is a comparison of oxygen ion conductivities of LMS predicted by *ab initio* studies to experimental results. (e)  $D_{chem}$  and  $k_{chem}$  of LMS comparing with  $\text{La}_2\text{NiO}_{4+\delta}$  (LaNiO),  $\text{La}_{0.5}\text{Sr}_{0.5}\text{FeO}_3$  (LSF),  $\text{La}_{0.5}\text{Sr}_{0.5}\text{CoO}_3$  (LSC),  $\text{La}_{0.6}\text{Sr}_{0.4}\text{Co}_{0.2}\text{Fe}_{0.8}\text{O}_3$  (LSCF),  $\text{Ba}_{0.5}\text{Sr}_{0.5}\text{Co}_{0.8}\text{Fe}_{0.2}\text{O}_3$  (BSCF), and  $\text{BaCo}_{0.7}\text{Fe}_{0.22}\text{Y}_{0.08}\text{O}_{3-\delta}$  (BCFY).

## Methods

### 1. Descriptor screening approach

Step (1) Free space. Crystallographic information files (CIF files) from the Materials Project database were used to calculate the free volume for forming interstitials. DFT-computed structures in the Materials Project are first analyzed using the Voronoi analysis method implemented in pymatgen<sup>1</sup> to find the potential interstitial sites. Distance from the interstitial site to its nearest neighboring cations  $d_c$  and anions  $d_a$  were used as the descriptor of the free volume needed for an interstitial oxygen anion  $O^{2-}$ . Specifically, the screening criteria were established as  $d_c \geq 0.99 \text{ \AA}$  and  $d_a \geq 0.88 \text{ \AA}$ . The distance criteria applied above were established by taking the minimum distances observed for the interstitial oxygens in Ruddlesden-Popper  $La_2NiO_4$  and apatite  $La_{10}Si_6O_{27}$ , which were taken as a guide to determine if there is sufficient room for an interstitial oxygen anion  $O^{2-}$  in the material. Interstitial sites that met the screening criteria were identified as reasonable interstitial oxygen sites  $O_i$  for the next step and only structures with such  $O_i$  sites were retained. After step (1), 16,455 compounds were retained, and the search space was reduced by 52%.

Step (2) Short hop distance. The minimum distance between the two nearest neighboring  $O_i$  sites from step (1) was used as the criterion representing the hop distance. Only materials with this distance  $\leq 3 \text{ \AA}$  were retained. This distance was chosen based on the shortest hop distance of interstitial oxygen in Ruddlesden-Popper  $La_2NiO_4$  and apatite  $La_{10}Si_6O_{27}$ , for which the hop distance is  $\sim 2.8 \text{ \AA}$  and  $\sim 2.7 \text{ \AA}$ , respectively. After step (2), 9,477 compounds were retained, and the search space was reduced by 72%.

Step (3) thermodynamic stability. Materials stability was assessed based on energy relative to the convex hull ( $E_{hull}$ ) as computed by the Materials Project. Only compounds with  $E_{hull} < 100 \text{ meV/atom}$  (closed system) and  $E_{hull} < 200 \text{ meV/atom}$  (system open to  $P(O_2) = 0.2 \text{ atm}$  and  $T = 300 \text{ K}$ ) were retained. These thresholds were chosen to be simple round numbers and within a few tens of meV/atom above the cutoffs that

identify the Ruddlesden-Popper  $La_2NiO_4$  and apatite  $La_{10}Si_6O_{27}$  as acceptably stable, since these are well-studied interstitial oxygen conductors known to be reasonably stable under many device conditions. Ruddlesden-Popper  $La_2NiO_4$  has  $E_{hull} = 76 \text{ meV}$  (closed system) and  $E_{hull} = 94 \text{ meV}$  (open to  $P(O_2) = 0.2 \text{ atm}$  and  $T = 300 \text{ K}$ ), and apatite  $La_{10}Si_6O_{27}$  has  $E_{hull} = 54 \text{ meV}$  (closed system) and  $E_{hull} = 169 \text{ meV}$  (open to  $P(O_2) = 0.2 \text{ atm}$  and  $T = 300 \text{ K}$ ), respectively.

Step (4) oxidizability. The valence state of each site was predicted by the Bond Valence analysis<sup>2</sup> module incorporated in pymatgen. To ensure the redox process of including additional oxygen into the materials with a low barrier, we proposed that the redox property from the cations is critical. If the valence state of a cation is smaller than its maximum oxidation state, for example, the Mn atom is at 2+ instead 7+, there are free valence electrons associated with this cation, and the compound has high redox potential and thus can be easily oxidized. Oxidizability is assessed by calculating the sum of the differences between the highest valence state and the actual valence state of each cation ion. Only compounds predicted to have oxidizable cations were retained.

Step (5) synthesizability. Materials are checked for whether it was reported as being synthesized at least once in the Inorganic Crystal Structure Database (ICSD)<sup>3</sup>. Compounds were retained only if the structure has an entry of experimental data in ICSD. After steps (3)-(5), only 519 compounds were retained, and the search space was reduced by 98.5%.

Step (6) Structure similarity analysis. For the remaining 519 compounds, a structure similarity analysis<sup>4</sup> assessed based on local coordination information from all sites in two structures was performed to group these compounds into 345 structural families. One candidate for each structure group was selected for further validation with *ab initio* studies. The selection of the candidate material followed a two-step process. First, the candidate was selected from the top of the stability ranking. If multiple materials shared the same level of stability, the candidate was subsequently selected by its oxidizability ranking.

## 2. *Ab initio* simulation screening approach

Step (7) Formation energy ( $E_f$ ). Density functional theory (DFT) calculations were used to calculate the formation energy ( $E_f$ ). The interstitial site with the largest free space is calculated. Structure optimization was performed for the bulk structures from the Materials Project. Supercells were built from the relaxed bulk structure with an approximately minimum length of 8 Å along each direction to minimize defect self-interaction. Formation energy was calculated by  $E_f = E_{(\text{supercell with O}_i)} - E_{(\text{supercell})} - \mu_{\text{O}}$  (1), where the  $\mu_{\text{O}}$  is the oxygen chemical potential under air condition. The O chemical potential was calculated by using a combination of DFT calculated total energies and experimental thermodynamic data for O<sub>2</sub> gas at air condition<sup>5</sup> with the following form<sup>6</sup>

$$\mu_{\text{O}} = \frac{1}{2} \left[ E_{\text{O}_2}^{\text{VASP}} + \Delta h_{\text{O}_2}^0 + H(T, P^0) - H(T^0, P^0) - TS(T, P^0) + kT \ln \left( \frac{P}{P^0} \right) - \left( G_{\text{O}_2}^{\text{s,vib}}(T) - H_{\text{O}_2}^{\text{s,vib}}(T^0) \right) \right] (2),$$

where  $E_{\text{O}_2}^{\text{VASP}}$  is the *ab initio* calculated energy of an O<sub>2</sub> gas molecule,  $\Delta h_{\text{O}_2}^0$  is a numerical correction that takes into account the temperature increase of O<sub>2</sub> gas from 0 K to  $T^0$ , the contribution to the enthalpy at  $T^0$  when oxygen is in the solid phase, and the numerical error in overbinding of the O<sub>2</sub> molecule in DFT.  $\Delta h_{\text{O}_2}^0$  is obtained from comparing calculated formation energies and experimental formation enthalpies of numerous oxides, which is a widely used method to avoid the well-known overbinding error of the O<sub>2</sub> molecule from DFT.<sup>7,8</sup> We used  $\Delta h_{\text{O}_2}^0 = 0.68$  eV/O from Ref. 8.  $H(T, P^0)$  and  $H(T^0, P^0)$  are the gas enthalpy values at standard and general temperatures  $T^0$  and  $T$ , respectively. In this case,  $T^0$  is 298 K and  $T$  refers to the room temperature 300K.  $TS(T, P^0)$  is the gas entropy, and the logarithmic term is the adjustment of the chemical potential for arbitrary pressure, where  $P$  and  $P^0$  are the referenced pressure and the standard pressure, respectively. In this case, the referenced pressure is 0.2 atm. The  $\left( G_{\text{O}_2}^{\text{s,vib}}(T) - H_{\text{O}_2}^{\text{s,vib}}(T^0) \right)$  term accounts for the solid phase vibrations, which are

approximated with an Einstein model with an Einstein temperature of 500 K.<sup>9</sup>

Step (8) Migration barrier  $E_m$ . *Ab initio* molecular dynamics (AIMD) was performed at 2000K for 30ps for the remaining 80 compounds to have an initial evaluation of the migration barrier  $E_m$ . We used this initial run to observe the AIMD trajectories for hopping times and estimate the migration barrier based on the hop rate  $r$

$$r = \nu e^{\left( \frac{-E_m}{k_b T} \right)} (3),$$

where  $\nu$  is the attempt frequency, estimated as  $5 \times 10^{12} \text{ s}^{-1}$ ,  $k_b$  is the Boltzmann constant, and  $T$  is the temperature, respectively. The hop rate  $r$  was observed from the AIMD simulation, and an initial estimation for  $E_m$  could be determined. The hop rate of 0.033/ps, i.e., 1 hop observed within 30ps AIMD simulation, corresponds to a migration barrier of 0.86 eV. Materials that have at least 1 hop observed within 30ps at 2000K, were selected for further DFT studies with long AIMD runs at different temperatures to calculate oxygen tracer diffusion coefficients, which were fit to an Arrhenius form  $Ae^{E_m/kT}$ .

All the calculations in this screening approach were performed with DFT using the Vienna *ab Initio* Simulation Package (VASP) code.<sup>10</sup> The generalized gradient approximation exchange-correlation functional Perdew, Burke, and Ernzerhof (GGA-PBE)<sup>11</sup> and projector augmented wave method (PAW)<sup>12</sup> were used for the effective potential for all atoms. The valence electron configuration of the La, Mn, Si, and O atoms utilized in all calculations were  $5s^2 5p^6 6s^2 4d^1$ ,  $3p^6 4s^2 3d^5$ ,  $3s^2 3p^2$ , and  $2s^2 2p^4$ , respectively. The plane wave cutoff energy was 520 eV and spin-polarized calculations were performed. For the defect formation energy calculations, the stopping criteria for total energy calculations were 0.01 meV/cell for the electronic relaxation and 0.05 eV/Å for ionic relaxation, respectively. K-point meshes were automatically generated based on the structural volume with a k points density of  $0.04/\text{\AA}^3$  to ensure calculation accuracy. For the AIMD simulations were performed using gamma-point-only sampling of k-space. The structure was first heated up to 2000K within 0.3 ps in the NVT ensemble using the Andersen thermostat, and

then simulated in the NVT ensemble using a Nosé–Hoover thermostat<sup>13,14</sup> for 30ps.

### 3. AIMD simulation of $O_i$ diffusion in $\text{La}_4\text{Mn}_5\text{Si}_4\text{O}_{22+\delta}$

With approximately 2%  $O_i$  concentration, the oxygen ion diffusivity in  $\text{La}_4\text{Mn}_5\text{Si}_4\text{O}_{22+\delta}$  was studied by *ab initio* molecular dynamics (AIMD) simulation at the temperature from 1000K to 2200K, with a step of 200K. The structure was first heated up to 2000K within 0.3 ps in the NVT ensemble using the Andersen thermostat, and then simulated in the NVT ensemble using a Nosé–Hoover thermostat<sup>13,14</sup> at each temperature state. For each temperature, we performed 10 independent AIMD simulation trajectories with different initial seeds. For each temperature, these 10 AIMD trajectories spanned a range of time length, with approximate minimum simulation times of 90ps at 2200K, 105ps from 1400K to 2000K, 150ps at 1200K, and 190ps at 1000K, respectively. The longer times at lower temperatures were used to obtain well-converged results. No effort was made to correct for thermal expansion as it was assumed the effect would be small. The tracer diffusion coefficient  $D^*$  within a simulation time  $t$  was evaluated using the mean squared displacement (MSD) by the Einstein relation

$$D^* = \frac{1}{2dt} \langle \text{MSD} \rangle \quad (4),$$

where  $d=2$  is the dimension of the system as interstitial oxygen diffuses within the sorosilicate layer, and  $t$  is the simulation time. To enhance the statistical reliability of the diffusivity calculations from AIMD simulations, we performed a procedure fitting the Einstein relation of the MSD– $\Delta t$  curve to minimize the fitting errors. The approach involves partitioning a long-time AIMD trajectory into shorter-time ( $\Delta t$ ) segments, then the diffusivity for each of these shorter-time ( $\Delta t$ ) segments was calculated. This methodology was designed to exclude the ballistic region at small  $\Delta t$  and the poor statistic at large  $\Delta t$ .<sup>15</sup> We have chosen  $\Delta t$  of 60ps at T=2200K, 90ps at T=1400 to 2000K, and 120ps at T=1000 to 1200K, respectively. For each trajectory, we calculated a set of diffusivities within time intervals  $[t_i, t_i+\Delta t]$ , where  $t_i = [0\text{ps}, 1.2\text{ps}, 2.4\text{ps}, 3.6\text{ps}, \dots, (t-\Delta t)]$ . As

these values are highly correlated, we kept only values that are separated by at least the correlation time, which was calculated by the autocorrelation method described in reference<sup>16</sup>. We denote the diffusion coefficient for one partition  $i$ , of one AIMD trajectory  $j$ , at one temperature  $T$ , by  $D_{T,i,j}$ . The mean of the diffusivities calculated on these partitions was then calculated and used as the best estimate of the diffusion coefficient for the AIMD trajectory  $j$ , denoted  $D_{T,j} = \frac{1}{n} \sum_{i=1}^n D_{T,i,j}$ . Here  $n$  is the number of partitions, which typically ranges between approximately 10 to 20. We also calculated the standard deviation of these partition values to provide an error estimate for  $D_{T,j}$  but this is a qualitative guide that estimates the error due to the correlation introduced by using overlapping data in determining each  $D_{T,i,j}$ . Therefore, these error estimates were not used for any additional statistical analysis. As described above, at each temperature, we have 10  $D_{T,j}$  values ( $j = \{1,2,3, \dots, 10\}$ ) from 10 independent AIMD simulations. Then, we calculated the mean and standard deviation of the 10 entirely uncorrelated  $D_{T,j}$  values to obtain

$$D_T = \frac{1}{m} \sum_{j=1}^m D_{T,j} \quad (5),$$

$$D_T^{stddev} = \sqrt{\frac{1}{m-1} \sum_{j=1}^m (D_{T,j} - D_T)^2} \quad (6), \text{ and}$$

$$D_T^{sem} = D_T^{stddev} / \sqrt{m} \quad (7),$$

where  $m = 10$ ,  $D_T$  is the diffusivity at temperature  $T$ ,  $D_T^{stddev}$  represents the standard deviation of  $D_T$ , and  $D_T^{sem}$  represents the standard error of  $D_T$ .  $D_T$  and  $D_T^{sem}$  were utilized in the Arrhenius fitting for the migration barrier.

Then, the migration barrier was calculated by fitting the Arrhenius relationship using the diffusion coefficient at temperatures from 1000K to 2200K by

$$D = D_0 e^{\left(\frac{-E_m}{k_b T}\right)} \quad (7),$$

where  $D_0$  is the pre-exponential factor,  $k_b$  is the Boltzmann constant, and  $T$  is the temperature.

### 4. ML-IPMD simulations.

Machine learning interatomic potential (ML-IP) was trained by the moment tensor potential (MTP) method<sup>17,18</sup>. The training data were obtained from the AIMD trajectories from

1000K to 2600K with an interval of 200K. For each temperature, we collected 200 structures with a time interval of 0.12ps to cast aside similar structures. An optimized MTP is then obtained by minimizing the errors in the predicted energies, forces, and stresses with respect to the DFT data. We set the weights of 100:1:0 to the energy, force, and stress data points, following previous works.<sup>19,20</sup> The radius cutoff was set to be 5.0 Å, a typical value used in previously reported MTPs, and the maximum level of the basis functions is set to be 20. All the training and evaluations were performed using the Machine-Learning Interatomic Potentials (MLIP) package.<sup>21</sup> Classical MD simulations were performed using the trained MTP. The time step was set to 1 fs, and the total simulation time was 1 ns for temperatures above 1200K, 5 ns at 1000K, 20ns at 800K, and 100ns at 600K, respectively.

### 5. Synthesis.

Stoichiometric quantities of highly pure La<sub>2</sub>O<sub>3</sub> (Alfa Aesar, 99.99 %), MnO<sub>2</sub> (Acros Organics, > 99.99 %), and SiO<sub>2</sub> (Alfa Aesar, 99.9 %) were mixed with KCl (Alfa Aesar, 99 – 100.5 %) flux. The flux-to-reactants molar ratio was 28.5:1 (mass ratio was 1.6:1). The reaction mixture was heated in a covered alumina crucible (30ml) at 900 °C for 6 days. The sample was slowly cooled down to 500 °C at a cooling rate of 20 °C/h and then further cooled down to room temperature at a cooling rate of 95 °C/h. The resultant mixture was washed with deionized water several times to remove the KCl flux, and then the obtained powder was dried on a hot plate at 120 °C in air. The LMS powder was grounded to fine powder in acetone medium using a porcelain mortar-pestle and pelletized in a rectangular bar using polyvinyl alcohol as binder and sintered at 1050 °C for 24 h.

### 6. Characterization.

The structural characterization of the LMS powder and pellet sample was performed using room temperature X-ray diffraction (XRD) technique using Cu-K $\alpha$  source (Bruker D8 Discovery) followed by Rietveld refinement using Fullprof code.<sup>22</sup> The Field effect scanning electron microscopy (FESEM) image of the pellet was collected using a high-resolution microscope (Zeiss 1530). The UV-vis diffuse reflectance of the

LMS pellet was measured using a spectrophotometer (Perkin Elmer Lambda 19 UV/Vis/NIR) and the optical band gap was determined using the Kubelka Munk equation<sup>23</sup> and Tauc plot.<sup>24</sup> X-ray photoemission spectroscopy analysis was performed on the sintered LMS pellet surface using a Thermo K-Alpha X-ray photoelectron spectrometer (Al-ka source). The pellet surface was cleaned by Ar sputtering inside the XPS chamber at ultra-high vacuum ( $\sim 10^{-9}$  torr). The spot size of the X-ray beam was 400 micrometers.

### 7. EPMA Analysis.

The chemical composition of the polished LMS pellet was measured using a CAMECA SX-Five FE-EPMA operated at 12 kV accelerating voltage and 20 nA beam current. The lowest possible accelerating voltage was selected that would minimize activation volume while also providing adequate overvoltage for excitation of Mn K $\alpha$ . Samples were mounted in epoxy and polished with colloidal alumina suspension. Samples and standards were coated with 1 nm Ir immediately prior to analysis. The O K $\alpha$  X-rays were measured with PCO crystal (2d=47.12Å), Si K $\alpha$  with LTAP (thallium acid phthalate, large format), Mn K $\alpha$  with LLIF (lithium fluoride, large format), and La L $\alpha$  with LPET (pentaerythritol, large format). Pulse height analysis was operated in differential mode for O and Si to avoid high order reflections from La. Spectral resolution of the PCO crystal on 160 mm radius Rowland circle was adequate to resolve O Ka peaks from interference with Mn L/ without requiring direct interference correction. Measurements included a 20s peak counting time and 10s counting time for each high and low background position. The electron beam was fully focused for spot measurements, with a practical spot diameter of approximately 250 nm. The accuracy of individual measurements was evaluated based on the quality of the analytical total. The average atomic percentage was determined from the analysis of 14 individual grains on the sample surface with <0.5 wt% standard deviation for each element and used to calculate the bulk atomic formula (**Table S6**).

### 8. Thermogravimetry analysis.

Thermogravimetric analysis (TGA) was performed in oxygen at the temperature range from 50 to 750 °C at a heating and cooling rate of 3 °C/ min using a TGA analyzer (TA Instruments Q500). The ground LMS powder was heated in two cycles to remove any adsorbed species. The third cycle is plotted in **Fig. S7**. A small increase of the total mass of about 0.02 mg (corresponding to a change in  $\delta$  of about 0.1) was observed when heating (and a similar decrease when cooling) the LMS powder. These changes are close to the instrument's weight change sensitivity ( $\pm 0.01\text{mg}$ )<sup>25</sup> denoted as the shaded region in **Fig. S7**. Considering that the mass changes are close to the instrument's resolution, we do not think these changes are statistically meaningful and interpret these results to imply a negligible mass change and reasonably constant oxygen stoichiometric with heating/cooling (more quantitatively, less than 0.02 mg and less than  $\delta = 0.1$  mass and stoichiometry changes, respectively). A small mass correction (0.01% of total mass) was performed to compensate for the sudden mass jump at the beginning of the heating cycle. We speculate that this abrupt fluctuation is associated with the instrument heater as similar behavior was observed in other materials too. The structural stability of the sample was also confirmed by performing XRD analysis after the TGA measurements.

### 9. Conductivity measurement.

The total conductivity of the LMS was measured in air conditions by the conventional DC 4-probe method using a Keithley 6221 power supply and a 2182A nanovoltmeter. Pt wire and silver paste were used for the electrical connection. Pt wires were used as the current and voltage leads. The current leads were connected to the two ends of LMS pellet using Ag paste. The voltage leads were wrapped around the LMS pellet at equal distances from the two ends using Ag-paste filling the gap between the Pt wire and LMS pellet to ensure a good electrical connection. For all the conductivity measurements, we used the current in the range of 1 to 10  $\mu\text{A}$ .

Electronic conductivity was measured using Au as the ionic blocking electrode at the two ends of the polished LMS pellet.<sup>26</sup> We first

deposited Au (300 nm) on one cross-section of the LMS pellet using Au sputtering unit (Leica ACE600) and heated it at 600 °C for 2 hours, and then repeated for the other cross-section. Afterwards, we deposited a thick Au layer (approximately 200 microns) on both ends using high pure Au paste and heated it at 900 °C for 2 hours. Pseudo 4-probe method was used to measure the electronic conductivity, where both the current and voltage leads were connected to the Au electrode terminals.

The ionic conductivity measurement was performed using 8YSZ blocks as the electronic blocking electrode.<sup>26</sup> A schematic of the assembly was displayed in **Fig. S10** along with the details of the setup in the supplementary file. The ionic conductivity of LMS was measured in air from 600 to 750 °C. To measure the resistance at a particular temperature, we measured the voltage across the LMS pellet at different currents and determined the resistance from the linear region of the I-V curve as shown in **Fig. S12**. The non-linearity at the higher current region of the I-V curve indicates the presence of ionic conductivity in LMS.<sup>26</sup> Conductivity measurements were conducted on three LMS pellets, The averaged conductivity along with its standard deviation are displayed in **Fig. S9**.

### 10. Electrical conductivity relaxation (ECR).

ECR study was performed using LMS pellet of length  $\sim 15$  mm, width  $\sim 6$  mm and thickness  $\sim 0.6$  mm. A vertical and sealed alumina tube was used as the ECR chamber. The sintered LMS pellet was kept floating inside the chamber using 4 Pt-wires passing through a 4-bore alumina tube. The excess space of the ECR chamber was filled using alumina balls of average diameter of  $\sim 3$  mm to reduce the effective chamber volume for faster gas exchange. The same electrical connection method described in the total conductivity measurement was used. 21 % and 5 % oxygen balanced  $\text{N}_2$  gas with a total flow of 300 SCCM was used to create different  $\text{P}(\text{O}_2)$  conditions inside the chamber. A 4-way gas switching valve was installed for the fast gas switching at the sample chamber. Abrupt oxygen partial pressure was changed from 5 to 21 % and vice versa at 750, 700, 650 and 600 °C, and the transient conductivity was

measured. The normalized and fitted ECR data during the oxidation and reduction at different temperatures were shown in **Fig. S13a-b**. The value of  $D_{chem}$  and  $k_{chem}$  of LMS at a fixed temperature was determined as the average during oxidation and reduction at that temperature. The fitting details were presented in **SI Discussion 9**.

### 11. Fittings of experimental data

The experimental activation energy of oxygen ion conducting in LMS was fitted on three separate measurements conducted on three LMS pellets using the Arrhenius relation  $\sigma T = A_{\sigma} e^{(-\frac{E_A}{k_b T})}$ , from which the average activation is 0.78 eV with a standard deviation of 0.07 eV from the three LMS pellets.

The experimental activation energies of chemical oxygen diffusivity  $D_{chem}$  and surface exchange coefficient were obtained by fitting the Arrhenius relation  $D_{chem} = D_{chem}^0 e^{(-\frac{E_A}{k_b T})}$  and  $k_{chem} = k_{chem}^0 e^{(-\frac{E_A}{k_b T})}$ . The  $D_{chem}$  and  $k_{chem}$  were obtained from ECR analysis on one LMS pellet. The activation energy is  $0.70 \pm 0.01$  eV for  $D_{chem}$  and  $0.82 \pm 0.01$  eV for  $k_{chem}$ , respectively, where the error bars are the standard deviation, representing the goodness of fitting.

The experimental tracer diffusion coefficient  $D^*$  was derived using the equation  $D^* = H_R D_{\sigma}$ , where  $H_R$  is known as Haven ratio.  $D_{\sigma}$  is a derived quantity (often referred as self-diffusion coefficient, or jump diffusion coefficient, or charge diffusion coefficient) calculated by the Nernst-Einstein equation  $D_{\sigma} = \frac{\sigma RT}{c z^2 F^2}$ . In Nernst-Einstein equation,  $\sigma$  is the experimental conductivity,  $R$  is gas constant,  $T$  is temperature,  $c$  is the oxygen volume concentration calculated as  $c = \frac{22 + \delta}{V}$ , where  $\delta = 0.42$ . Additionally,  $z$  is the charge of oxygen ion (-2), and  $F$  is the faraday constant. The Haven ratio  $H_R$  was determined to be 1.54 from *ab initio* studies analysis in **SI Discussion 11**.

### Data availability

Source data and data that support the plots within this paper are available on Figshare.

<https://figshare.com/s/1a9489d7bb64bf473ff3>. Please refer to the readme.txt file in the repository for guidance.

### Acknowledgements

This work was funded by the US Department of Energy (DOE), Office of Science, Basic Energy Sciences (BES), under Award # DE-SC0020419. This work used the Extreme Science and Engineering Discovery Environment (XSEDE), which is supported by National Science Foundation Grant Number ACI-1548562.

### Author contributions

J.M. and S.S. have equal contributions to this work. R.J. and D.M. conceived and managed the project. J.M. performed the screening, *ab initio* calculations, and theoretical analyses with assistance from D.M. and R.J. S.S. performed the synthesis, characterization, conductivity, and kinetic measurements. J.L. helped with the ECR analysis and contributed to scientific discussions. W.O.N. performed the EPMA analysis. X.L. trained the machine learning interatomic potential. J.M. wrote the first version of the manuscript with input from S.S. R.J. and D.M. reviewed the manuscript. All authors have reviewed and commented on the manuscript.

### Competing interests

The authors declare no competing interests.

### Reference

1. Atsuyuki Okabe, Barry Boots, Kokichi Sugihara, S. N. C. *Spatial tessellations: concepts and applications of Voronoi diagrams*. (John Wiley, 2000).
2. O'Keefe, M. & Brese, N. E. Atom sizes and bond lengths in molecules and crystals. *J. Am. Chem. Soc.* **113**, 3226–3229 (1991).
3. Belsky, A., Hellenbrandt, M., Karen, V. L. & Luksch, P. New developments in the Inorganic Crystal Structure Database (ICSD): accessibility in support of materials research and design. *Acta Crystallographica Section B* **58**, 364–369 (2002).
4. Pan, H. *et al.* Benchmarking Coordination Number Prediction Algorithms on Inorganic

- Crystal Structures. *Inorg. Chem.* **60**, 1590–1603 (2021).
5. P.J. Linstrom and W.G. Mallard, Eds. NIST Chemistry WebBook, NIST Standard Reference Database Number 69. *National Institute of Standards and Technology, Gaithersburg MD, 20899* (2023).
  6. Jacobs, R. M., Booske, J. H. & Morgan, D. Intrinsic defects and conduction characteristics of  $\text{Sc}_2\text{O}_3$  in thermionic cathode systems. *Phys. Rev. B* **86**, 1–10 (2012).
  7. Hine, N. D. M., Frensch, K., Foulkes, W. M. C. & Finnis, M. W. Supercell size scaling of density functional theory formation energies of charged defects. *Phys. Rev. B* **79**, 1–13 (2009).
  8. Wang, L., Maxisch, T. & Ceder, G. Oxidation energies of transition metal oxides within the GGA+U framework. *Phys. Rev. B* **73**, 195107 (2006).
  9. Lee, Y.-L., Kleis, J., Rossmeisl, J. & Morgan, D. Ab initio energetics of  $\text{LaBO}_3(001)$  (B=Mn, Fe, Co, and Ni) for solid oxide fuel cell cathodes. *Phys. Rev. B* **80**, 224101 (2009).
  10. Kresse, G. & Furthmüller, J. Efficient iterative schemes for ab initio total-energy calculations using a plane-wave basis set. *Phys. Rev. B* **54**, 11169–11186 (1996).
  11. Perdew, J., Burke, K. & Ernzerhof, M. Generalized Gradient Approximation Made Simple. *Phys. Rev. Lett.* **77**, 3865–3868 (1996).
  12. Kresse, G. & Joubert, D. From ultrasoft pseudopotentials to the projector augmented-wave method. *Phys. Rev. B* **59**, 1758–1775 (1999).
  13. Shuichi, N. Constant Temperature Molecular Dynamics Methods. *Prog. Theor. Phys. Suppl.* **103**, 1–46 (1991).
  14. Hoover, W. G. Canonical dynamics: Equilibrium phase-space distributions. *Phys. Rev. A* **31**, 1695–1697 (1985).
  15. He, X., Zhu, Y., Epstein, A. & Mo, Y. Statistical variances of diffusional properties from ab initio molecular dynamics simulations. *npj Comput. Mater.* **4**, 18 (2018).
  16. Box, G. E. P. & Jenkins, G. M. *Time Series Analysis: Forecasting and Control*. (Holden-Day, 1976).
  17. Shapeev, A. V. Moment Tensor Potentials: A Class of Systematically Improvable Interatomic Potentials. *Multiscale Modeling and Simulation* **14**, 1153–1173 (2016).
  18. Gubaev, K., Podryabinkin, E. V., Hart, G. L. W. & Shapeev, A. V. Accelerating high-throughput searches for new alloys with active learning of interatomic potentials. *Comput. Mater. Sci.* **156**, 148–156 (2019).
  19. Zuo, Y. *et al.* Performance and Cost Assessment of Machine Learning Interatomic Potentials. *J. Phys. Chem. A* **124**, 731–745 (2020).
  20. Li, X.-G., Chen, C., Zheng, H., Zuo, Y. & Ong, S. P. Complex strengthening mechanisms in the NbMoTaW multi-principal element alloy. *npj Comput. Mater.* **6**, 70 (2020).
  21. Novikov, I. S., Gubaev, K., Podryabinkin, E. V & Shapeev, A. V. The MLIP package: moment tensor potentials with MPI and active learning. *Mach. Learn. Sci. Technol.* **2**, 025002 (2021).
  22. Rodríguez-Carvajal, J. Recent advances in magnetic structure determination by neutron powder diffraction. *Phys. B Condens. Matter.* **192**, 55–69 (1993).
  23. Sangiorgi, N., Aversa, L., Tatti, R., Verucchi, R. & Sanson, A. Spectrophotometric method for optical band gap and electronic transitions determination of semiconductor materials. *Opt. Mater.* **64**, 18–25 (2017).
  24. Tauc, J., Grigorovici, R. & Vancu, A. Optical Properties and Electronic Structure of Amorphous Germanium. *physica status solidi (b)* **15**, 627–637 (1966).
  25. TA Instruments Q500. <https://wcnt.wisc.edu/thermogravimetric-analysis/>
  26. Lei, C., Simpson, M. F. & Virkar, A. V. Investigation of Ion and Electron Conduction in the Mixed Ionic-Electronic Conductor- La-Sr-Co-Fe-Oxide (LSCF) Using Alternating Current (AC) and Direct Current (DC) Techniques. *J. Electrochem. Soc.* **169**, 14506 (2022).

# Computational Discovery of Fast Interstitial Oxygen Conductors

Jun Meng<sup>1,4</sup>, Md Sariful Sheikh<sup>1,4</sup>, Ryan Jacobs<sup>1</sup>, Jian Liu<sup>2</sup>, William O. Nachlas<sup>3</sup>, Xiangguo Li<sup>1</sup>, Dane Morgan<sup>1,\*</sup>

<sup>1</sup> Department of Materials Science and Engineering, University of Wisconsin Madison, Madison, WI, USA.

<sup>2</sup> DOE National Energy Technology Laboratory, Morgantown, WV, USA.

<sup>3</sup> Department of Geoscience, University of Wisconsin Madison, Madison, WI, USA.

<sup>4</sup> These authors contributed equally: Jun Meng, Md Sariful Sheikh. E-mails: [ddmorgan@wisc.edu](mailto:ddmorgan@wisc.edu).

## Table of Contents

### Supplementary Tables

<b>Table S1.</b> Materials list with <i>ab initio</i> calculated interstitial oxygen formation energy $E_f \leq 0.3$ eV under atmosphere condition (T=300 K, P(O <sub>2</sub> )=0.2 atm). .....	3
<b>Table S2.</b> Materials list studied by initial evaluation by 30ps <i>ab initio</i> molecular dynamics simulation at 2000K. ....	4
<b>Table S3.</b> Lattice parameter and optical band gap of bulk La <sub>4</sub> Mn <sub>5</sub> Si <sub>4</sub> O <sub>22</sub> calculated by different exchange and correlation functionals compared to available experimental data, along with the calculated interstitial oxygen formation energy $E_f$ in bulk La <sub>4</sub> Mn <sub>5</sub> Si <sub>4</sub> O <sub>22+<math>\delta</math></sub> under atmosphere environment (T=300 K, P(O <sub>2</sub> )=0.2 atm).....	4
<b>Table S4.</b> Comparison of the lattice vectors of La <sub>4</sub> Mn <sub>5</sub> Si <sub>4</sub> O <sub>22+<math>\delta</math></sub> obtained from the Rietveld refinement of XRD data, and previous report (PDF: 04-011-1866). ....	5
<b>Table S5.</b> Rietveld refined lattice positions of La <sub>4</sub> Mn <sub>5</sub> Si <sub>4</sub> O <sub>22+<math>\delta</math></sub> . ....	5
<b>Table S6.</b> Atomic percentage measured by the electron probe micro-analyzer (EPMA) and the derived formula from EPMA and Iodometric titration analysis compared with the ideal results. ....	6

### Supplementary Figures

<b>Figure S1.</b> Configuration of the most stable sites of interstitial oxygen O <sub>i</sub> and vacancy oxygen V <sub>O</sub> in La <sub>4</sub> Mn <sub>5</sub> Si <sub>4</sub> O <sub>22</sub> . ....	6
<b>Figure S2.</b> Energy landscape of the interstitial diffusion and interstitialcy diffusion calculated by the climbing image nudged elastic band (CI-NEB) method using (a) SCAN and (b) GGA-PBE functional, respectively. ....	6
<b>Figure S3.</b> Arrhenius plot of tracer diffusivity $D^*$ of oxygen predicted by <i>ab initio</i> molecular dynamics (AIMD) calculated by GGA-PBE functional and machine learning trained interatomic potential molecular dynamics (ML-IPMD) simulation.....	7
<b>Figure S4.</b> Comparison of the machine learning interatomic potential predicted energy and force on each atom with the DFT results. ....	7
<b>Figure S5.</b> The field emission electron microscope (FESEM) image of dense La <sub>4</sub> Mn <sub>4.69</sub> Si <sub>4.03</sub> O <sub>22.42</sub> (LMS) pellet sintered at 1050 °C for 24h. ....	8
<b>Figure S6.</b> XPS survey spectrum of La <sub>4</sub> Mn <sub>4.69</sub> Si <sub>4.03</sub> O <sub>22.42</sub> (LMS). ....	8
<b>Figure S7.</b> Total mass change of LMS throughout the thermogravimetric analysis between 50 °C and 750 °C under a 1 atm O <sub>2</sub> environment.....	9

<b>Figure S8.</b> Diffuse reflectance spectroscopy of $\text{La}_4\text{Mn}_{4.69}\text{Si}_{4.03}\text{O}_{22.42}$ (LMS) pellet and the determined optical band gap. ....	9
<b>Figure S9.</b> Measured total conductivity, electronic conductivity, and ionic conductivity of $\text{La}_4\text{Mn}_{4.69}\text{Si}_{4.03}\text{O}_{22.42}$ (LMS). ....	10
<b>Figure S10.</b> A schematic of the ionic conductivity measurement method using the conventional DC 4-probe method with 8YSZ (8 mol% Yttria-Stabilized Zirconia) electron blocking on both ends. ....	10
<b>Figure S11.</b> Temperature-dependent ionic conductivity of $\text{La}_{0.6}\text{Sr}_{0.4}\text{Co}_{0.2}\text{Fe}_{0.8}\text{O}_{3-\delta}$ (LSCF) measured using 8YSZ (8 mol% Yttria-Stabilized Zirconia) electron blocking in this work compared with literature reported ionic conductivity of LSCF. ....	11
<b>Figure S12.</b> Current-voltage characteristics across LMS in Au/LSCF/YSZ/LMS/LSCF/YSZ/Au system at temperature from 600 to 750 °C. ....	12
<b>Figure S13.</b> Normalized and fitted electrical conductivity relaxation (ECR) data during oxidation and reduction at temperatures from 600 to 750 °C. The fitted $D_{\text{chem}}$ , $k_{\text{chem}}$ , and Bi-number during oxidation and reduction. The derived thermodynamic factor of LMS at temperature from 600 to 750 °C. ....	13
<b>Figure S14.</b> Room temperature X-ray diffraction (XRD) pattern of the LMS pellet before and after the electronic conductivity relaxation (ECR) study. ....	14
<b>Figure S15.</b> The tracer diffusion coefficient $D^*$ and the trace surface exchange coefficient $k^*$ of $\text{La}_4\text{Mn}_5\text{Si}_4\text{O}_{22+\delta}$ compared to the state-of-art materials. ....	14
<b>Figure S16.</b> (a) Arrhenius plot of tracer diffusion coefficient $D^*$ and charge diffusion coefficient $D_\sigma$ of oxygen derived from ab initio molecular dynamics (AIMD) with GGA-PBE functional. (b) The Haven ratio calculated by $D^*$ and $D_\sigma$ at each temperature.....	15

## Discussion

1. Database of experimental migration barrier of oxygen-ion conducting materials.....	15
2. Origin of the availability of electrons and structural flexibility across families of high-performing interstitial oxygen formers and conductors.....	16
3. Electrical property and defect formation energy with different DFT functionals.....	17
4. DFT studies of oxygen defects in $\text{La}_4\text{Mn}_5\text{Si}_4\text{O}_{22+\delta}$ . ....	18
5. Calculated spin state of $\text{La}_4\text{Mn}_5\text{Si}_4\text{O}_{22+\delta}$ .....	18
6. Climbing Image Nudged Elastic Band (CI-NEB) calculation. ....	19
7. Iodometric titration. ....	19
8. Preparation of the ionic conductivity measurement using YSZ blocks. ....	19
9. Fitting of the ECR data.....	20
10. Determination of average $D_{\text{chem}}$ and $k_{\text{chem}}$ of state-of-art materials from literatures.....	20
11. Conversion of ab initio diffusivity to conductivity and derivation of Haven ratio.....	21

## Reference

## Supplementary Tables

**Table S1.** Materials list with interstitial oxygen formation energy  $E_f \leq 0.3$  eV under atmosphere condition (T=300 K, P(O<sub>2</sub>)=0.2 atm) by *ab initio* calculation.

Materials-ID	Formula	$E_f$	Materials-ID	Formula	$E_f$
mp-23349	BiB3O6	-3.85	mp-772957	SrV4O10	-0.42
mp-1196071	Ba2Fe2O5	-3.51	mp-1196110	SrCuTe2O7	-0.34
mp-1204837	NaFe2Si6O15	-3.25	mp-1200170	Ba5Cr3O13	-0.34
mp-23356	Bi4B2O9	-2.73	mp-23446	GeBi2O5	-0.33
mp-555752	NaFe2Mo3O12	-2.68	mp-1195799	K2Fe2B2O7	-0.32
mp-1199587	Yb2VO5	-2.28	mp-556076	Sr2Co2O5	-0.30
mp-555924	Ca5Nb5O17	-2.10	mp-29189	VHg2O4	-0.29
mp-542931	Bi2B8O15	-2.05	mp-667343	Re2Hg5O10	-0.29
mp-559364	SrBi2B4O10	-2.00	mp-1204772	Co2As2O7	-0.27
mp-29508	LiMo3O9	-1.91	mp-558472	SrCu2B2O6	-0.23
mp-744682	Cr8Bi4O29	-1.69	mp-705159	K2Co2Mo3O12	-0.23
mp-29058	V3Bi6O16	-1.61	mp-563010	RbFeMo2O8	-0.20
mp-18907	Ca2MnAlO5	-1.55	mp-6496	Ba2NaCu3O6	-0.17
mp-1194512	V2Cu3O9	-1.47	mp-29112	CrHg5O6	-0.15
mp-630403	Ca2MnGaO5	-1.45	mp-18924	Sr3Fe2O6	-0.15
mp-558429	NaFe4Mo5O20	-1.37	mp-558751	CaBi2O4	-0.14
mp-19290	Mn2As2O7	-1.33	mp-6027	Ba2Ti2CuO6	-0.08
mp-559180	Ba2CuB2O6	-1.28	mp-704097	Sr6Co4Bi2O15	-0.05
mp-22113	Ca2Fe2O5	-1.25	mp-1203275	Co2AsO5	-0.04
mp-1003437	KMn2O4	-1.24	mp-1203433	Hg3AsO5	-0.04
mp-21926	SrFe2O4	-1.23	mp-647862	Cr2Mo3O12	-0.04
mp-753258	Li3CrO4	-1.13	mp-29048	SrBi2O4	0.00
mp-19165	BaFeSi4O10	-1.06	mp-1190373	K2V2CoO7	0.01
mp-29259	Bi2PdO4	-1.06	mp-554698	K10MnMo7O27	0.07
mp-556203	La8Ni4O17	-1.06	mp-17387	LiVAsO5	0.09
mp-20161	Na2CoGeO4	-0.91	mp-18893	Ca2Mn3O8	0.12
mp-18096	Na2CoSi4O10	-0.91	mp-559685	V2Cd4Te3O15	0.15
mp-18926	La3Ni2O7	-0.90	mp-1200219	V4Cr2O13	0.16
mp-21635	CeMn2Ge4O12	-0.87	mp-546111	Cr3AgO8	0.18
mp-1194618	Ba4Y2Fe2O11	-0.87	mp-560340	La2Pd2O5	0.18
mp-19228	K2MnV4O12	-0.82	mp-1200054	V4Fe2O13	0.19
mp-505042	CuBi2O4	-0.78	mp-541433	CdBi2O4	0.21
mp-550998	TiZnBi2O6	-0.73	mp-19142	Mn2V2O7	0.23
mp-541464	La4Mn5Si4O22	-0.70	mp-639811	KIrO3	0.24
mp-558316	La4Ni3O10	-0.69	mp-19395	MnO2	0.25

mp-37961	MgV3O8	-0.59	mp-1105484	Sm3FeO6	0.26
mp-18456	LaCrO4	-0.59	mp-560273	Cu3WO6	0.28
mp-557927	Na2SrV3O9	-0.56	mp-777667	LiV2O5	0.28
mp-1191696	LiCrMo2O8	-0.56	mp-553887	NaV2Bi3O10	0.28
mp-2669	Mo8O23	-0.52	mp-1194927	VCdCoO5	0.30
mp-22427	BaSrFe4O8	-0.51			

**Table S2.** Materials list studied by initial evaluation with 30ps *ab initio* molecular dynamic simulation at 2000K.  $E_m$  values are given in eV.

Materials-ID	Formula	Estimated $E_m$	Materials-ID	Formula	Estimated $E_m$
mp-651434	K2Mn2Mo3O12	0.36	mp-541433	CdBi2O4	structure not stable
mp-541464	La4Mn5Si4O22	0.44	mp-1003437	KMn2O4	structure not stable
mp-21635	CeMn2Ge4O12	0.45	mp-1200219	V4Cr2O13	structure not stable
mp-29259	Bi2PdO4	0.63	mp-19290	Mn2As2O7	structure not stable
mp-556076	Sr2Co2O5	0.62	mp-777667	LiV2O5	structure not stable
mp-19165	BaFeSi4O10	0.74	mp-753258	Li3CrO4	structure not stable
mp-18893	Ca2Mn3O8	0.8	mp-29112	CrHg5O6	structure not stable
mp-630403	Ca2MnGaO5	0.83	mp-1196110	SrCuTe2O7	structure not stable
mp-639811	KIrO3	0.86	mp-37961	MgV3O8	structure not stable
mp-647862	Cr2Mo3O12	>0.86	mp-19395	MnO2	structure not stable
mp-17387	LiVAsO5	>0.86	mp-563010	RbFeMo2O8	structure not stable
mp-6496	Ba2NaCu3O6	>0.86	mp-505042	CuBi2O4	structure not stable
mp-1191696	LiCrMo2O8	>0.86	mp-19142	Mn2V2O7	structure not stable
mp-2669	Mo8O23	structure not stable	mp-560273	Cu3WO6	structure not stable

**Table S3.** Lattice parameter and optical band gap of bulk La<sub>4</sub>Mn<sub>5</sub>Si<sub>4</sub>O<sub>22</sub> calculated using DFT with different exchange and correlation functionals compared to available experimental data, along with the calculated interstitial oxygen formation energy  $E_f$  in bulk La<sub>4</sub>Mn<sub>5</sub>Si<sub>4</sub>O<sub>22+ $\delta$</sub>  under atmosphere environment (T=300 K, P(O<sub>2</sub>)=0.2 atm).

Functional	a (Å)	b (Å)	c (Å)	$\alpha$ (°)	$\beta$ (°)	$\gamma$ (°)	Volume (Å <sup>3</sup> )	Optical Band gap (eV)	$E_f$ (eV)
<b>GGA</b>	5.64	7.60	11.33	73.94	75.59	68.22	427.18	0.44	-0.7
<b>GGA+U (U=3.9)</b>	5.67	7.62	11.35	74.08	75.52	68.14	431.83	1.02	1.13
<b>HSE (<math>\alpha=0.10</math>)</b>	5.73	7.53	11.28	73.74	75.28	67.62	426.19	0.73	0.73
<b>HSE (<math>\alpha=0.15</math>)</b>	5.71	7.52	11.27	73.78	75.29	67.66	423.96	1.11	1.02
<b>HSE (<math>\alpha=0.20</math>)</b>	5.70	7.51	11.25	73.81	75.31	67.70	421.53	1.54	1.31
<b>HSE (<math>\alpha=0.25</math>)</b>	5.69	7.50	11.23	73.83	75.32	67.71	419.47	1.93	1.57
<b>SCAN</b>	5.58	7.54	11.22	74.08	75.61	68.32	416.00	0.72	-0.11
<b>Experiment</b>	5.57	7.55	11.24	74.18	75.65	68.33	416.53	0.79	

**Table S4.** Comparison of the lattice vectors of  $\text{La}_4\text{Mn}_5\text{Si}_4\text{O}_{22+\delta}$  obtained from the Rietveld refinement of XRD data, and previous report (PDF: 04-011-1866).<sup>1</sup> The goodness-of-fit quantities are  $\chi^2=2.589$ , profile R-factor  $R_p=10.79$ , and weighted profile R-factor  $R_{wp}=12.65$ .

Parameter	Rietveld refined data	reference data
a (Å)	14.0461 (9) Å	14.024 Å
b (Å)	5.5836 (4) Å	5.571 Å
c (Å)	11.7299 (8) Å	11.703 Å
$\alpha$	90°	90°
$\beta$	114.3579 (13)°	114.34°
$\gamma$	90°	90°

**Table S5.** Rietveld refined lattice positions of  $\text{La}_4\text{Mn}_5\text{Si}_4\text{O}_{22+\delta}$ .

Elements	Wyckoff position	x	y	z
La1	4i	0.2375 (3)	0	0.2596 (3)
La2	4i	0.0521 (2)	0	0.7466 (3)
Mn1	4g	0	0.2585 (9)	0
Mn2	4i	0.2691 (5)	0.	-0.0013 (7)
Mn3	2d	0	0.5	0.5
Si1	4i	0.1700 (10)	0	0.5556 (10)
Si2	4i	0.4187 (13)	0	0.7505 (17)
O1	8j	0.0736 (12)	0.268 (2)	0.1769 (16)
O2	8j	0.2924 (11)	0.262 (3)	0.1160 (13)
O3	8j	0.3768 (15)	0.263 (3)	0.4068 (15)
O4	4i	0.0993 (10)	0	0.9910 (15)
O5	4i	0.4125 (20)	0	0.008 (3)
O6	4i	0.5062 (15)	0	0.7033 (19)
O7	4i	0.2784 (18)	0	0.624 (2)
O8	4i	0.1495 (17)	0	0.4060 (20)

**Table S6.** Atomic percentage value along with the standard deviation measured by the electron probe micro-analyzer (EPMA) and the derived formula from EPMA and Iodometric titration analysis compared with the ideal results.

	La	Mn	Si	O	Formula
Ideal	11.43%	14.29%	11.43%	62.86%	La <sub>4</sub> Mn <sub>5</sub> Si <sub>4</sub> O <sub>22</sub>
EPMA	11.39±0.14%	13.34±0.09%	11.46±0.29%	63.81±0.43%	La <sub>4</sub> Mn <sub>4.69</sub> Si <sub>4.03</sub> O <sub>22+0.42</sub>
Titration	11.39% (EPMA)	13.34% (EPMA)	11.46% (EPMA)	63.85±0.07 %	La <sub>4</sub> Mn <sub>4.69</sub> Si <sub>4.03</sub> O <sub>22+0.47</sub>

### Supplementary Figures

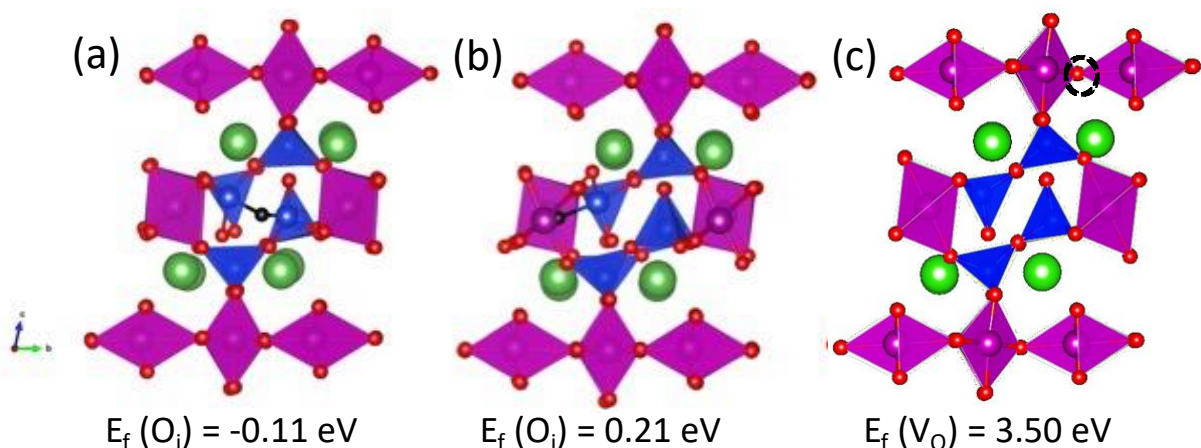


**Figure S1.** Configuration of the two most stable sites of interstitial oxygen  $O_i$  marked by black balls in (a) and (b), and the most stable vacancy oxygen  $V_O$  site marked by the black dashed circle in (c), along with the defect formation energy under air condition.

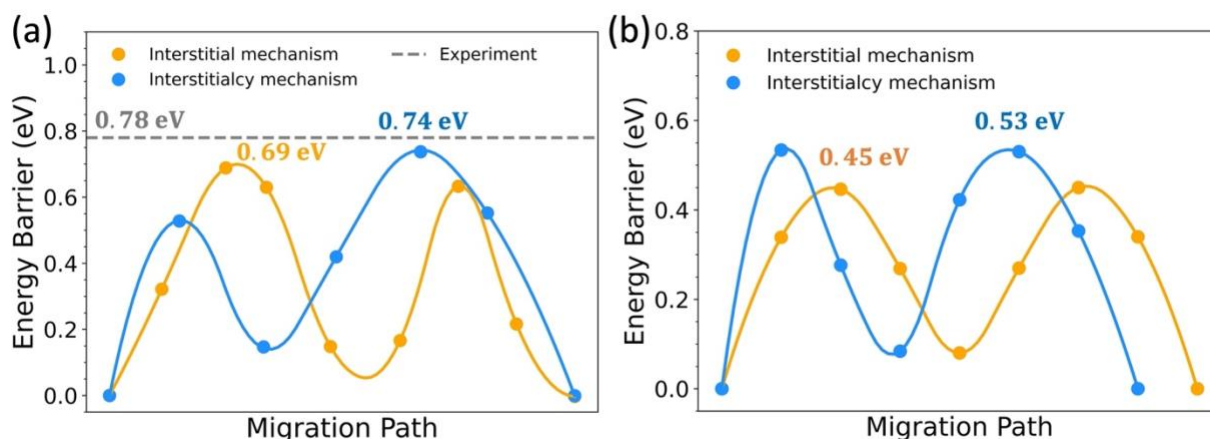


**Figure S2.** Energy landscape of the interstitial diffusion and interstitialcy diffusion calculated by the climbing image nudged elastic band (CI-NEB) method using (a) SCAN functional, and (b) GGA-PBE functional, respectively. The dashed line in (a) indicates the experimental activation energy for comparison.

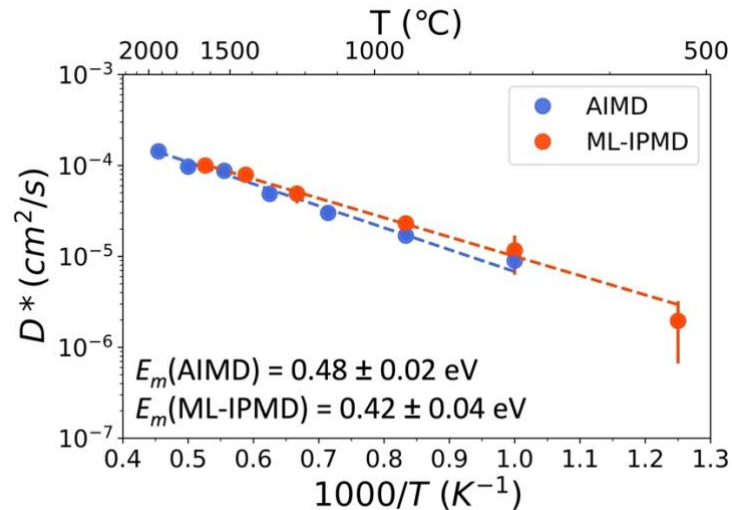


**Figure S3.** Arrhenius plot of tracer diffusivity  $D^*$  of oxygen predicted by *ab initio* molecular dynamics (AIMD) calculated by GGA-PBE functional and machine learning trained interatomic potential molecular dynamic (ML-IPMD) simulations. The error bars represent the standard error of the mean  $D^*$  (**Methods 3**).

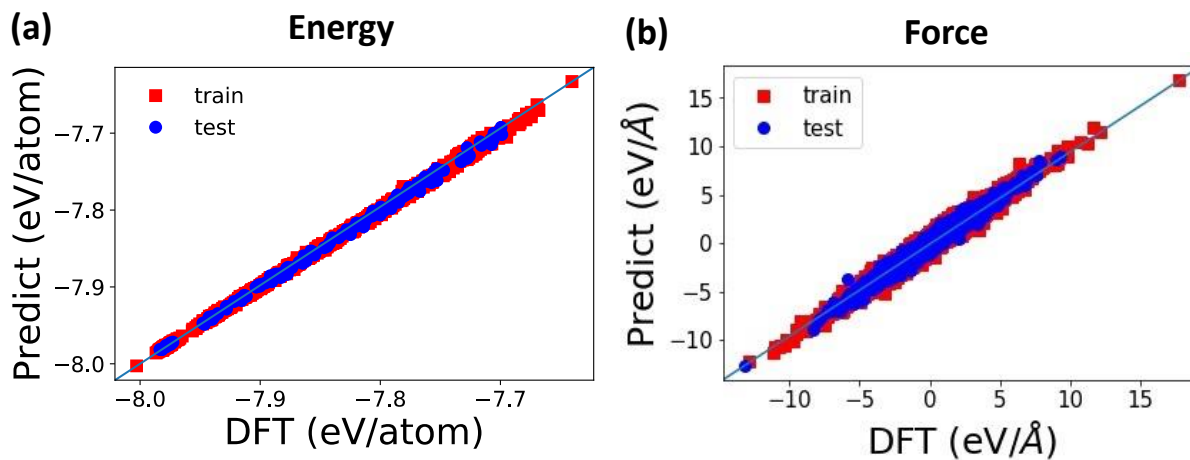


**Figure S4.** Comparison of the machine learning interatomic potential predicted (a) energy, and (b) force on each atom with the DFT results.

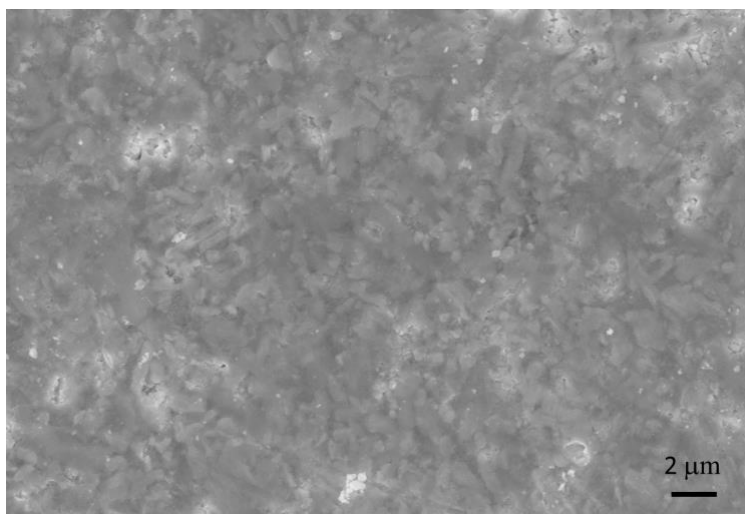


**Figure S5.** The field emission electron microscope (FESEM) image of dense La<sub>4</sub>Mn<sub>4.69</sub>Si<sub>4.03</sub>O<sub>22.42</sub> (LMS) pellet sintered at 1050 °C for 24h.

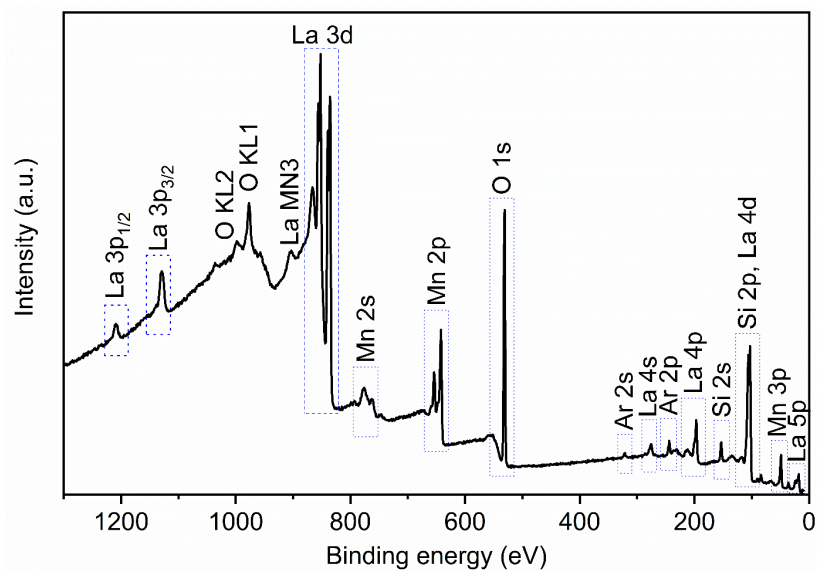


**Figure S6.** XPS survey spectrum of LMS, suggesting the presence of La, Mn, Si, and O atoms without presence of any detectable impurity elements.

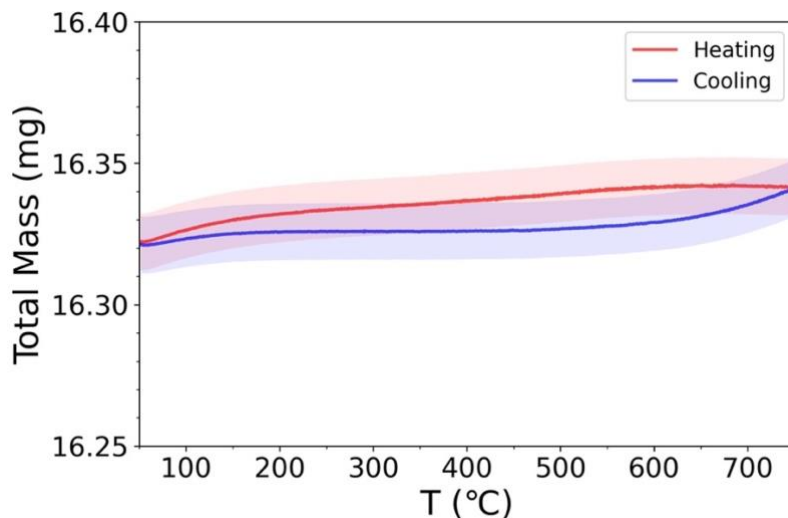


**Figure S7.** Total mass change of LMS throughout the thermogravimetric analysis between 50 °C and 750 °C under a 1 atm O<sub>2</sub> environment. The shaded region denotes the instrument's weight change sensitivity of ±0.01 mg.

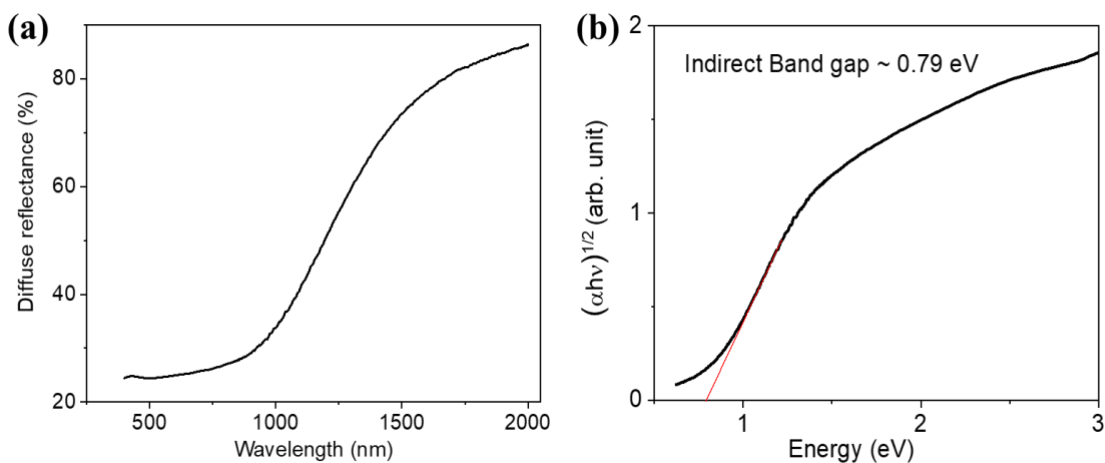


**Figure S8.** (a) Diffuse reflectance spectroscopy of LMS pellet. (b) The optical band gap of LMS was determined from the diffuse reflectance spectroscopy.

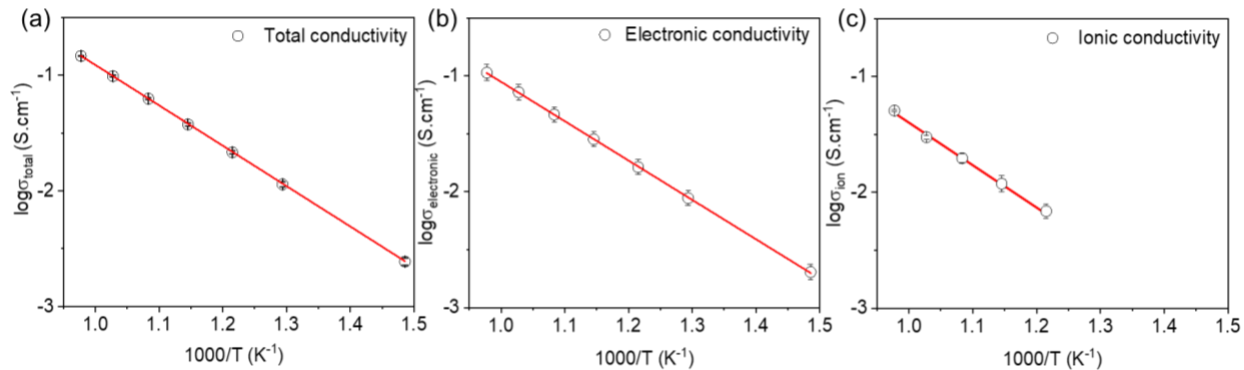


**Figure S9.** Measured (a) total conductivity, (b) electronic conductivity, and (c) ionic conductivity of the  $\text{La}_4\text{Mn}_{4.69}\text{Si}_{4.03}\text{O}_{22.42}$  sample. The error bars represent the standard deviation. The average conductivity and standard deviation were derived from the conductivity values measured on three different LMS samples. Some error bars are difficult to see as they are less than the size of the symbols.

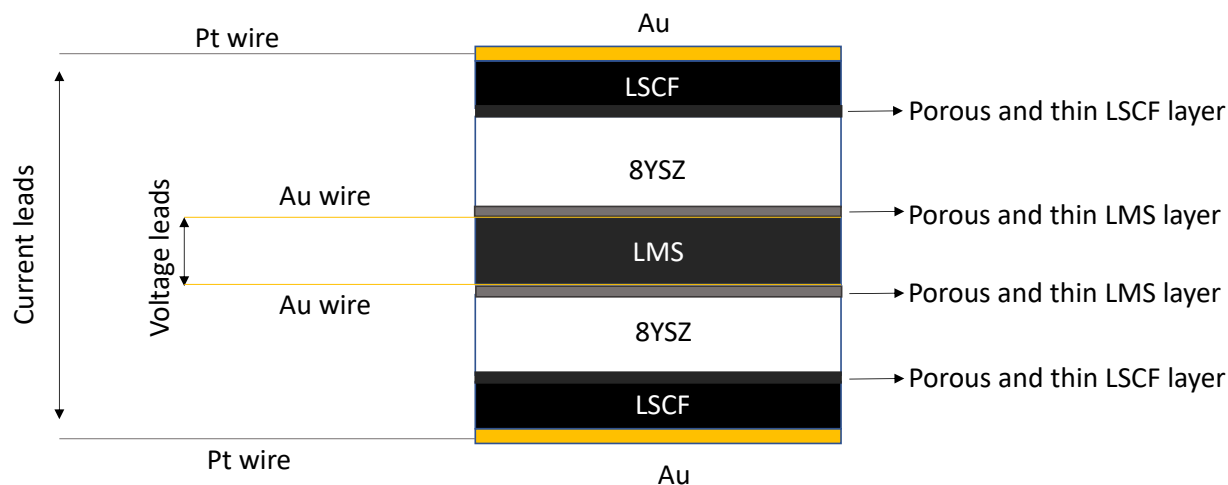


**Figure S10.** A schematic of the ionic conductivity measurement method using the conventional DC 4-probe method with 8YSZ (8 mol% Ytria-Stabilized Zirconia) electron blocking on both ends.

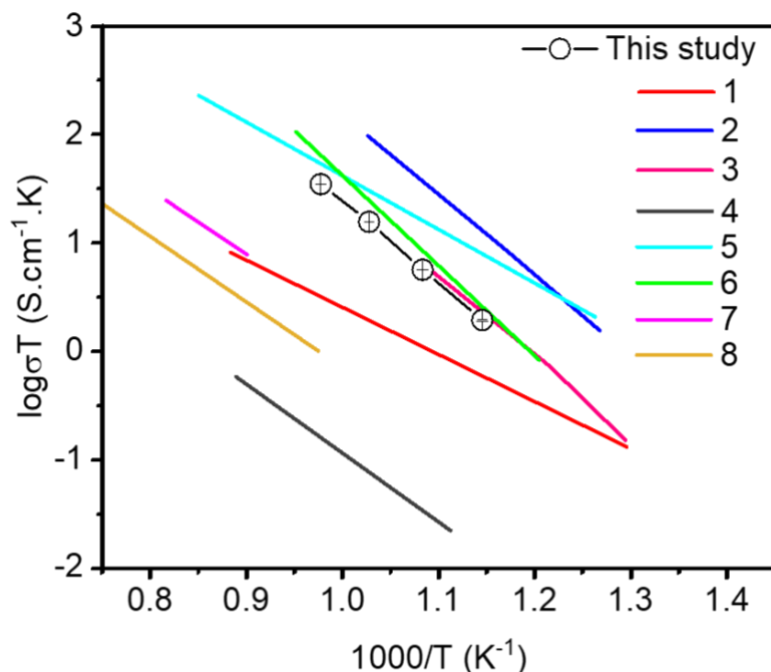


**Figure S11.** Temperature-dependent ionic conductivity of  $\text{La}_{0.6}\text{Sr}_{0.4}\text{Co}_{0.2}\text{Fe}_{0.8}\text{O}_{3-\delta}$  (LSCF) measured using 8YSZ (8 mol% Ytria-Stabilized Zirconia) electron blocking in this work compared with reported ionic conductivity of LSCF measured by impedance spectroscopy (1)  $\text{La}_{0.6}\text{Sr}_{0.4}\text{Co}_{0.2}\text{Fe}_{0.8}\text{O}_{3-\delta}$ ,<sup>2</sup> (2)  $\text{La}_{0.54}\text{Sr}_{0.44}\text{Co}_{0.2}\text{Fe}_{0.8}\text{O}_{3-\delta}$ ,<sup>3</sup> and (3)  $\text{La}_{0.6}\text{Sr}_{0.4}\text{Co}_{0.2}\text{Fe}_{0.8}\text{O}_{3-\delta}$ ;<sup>2</sup> 2-probe method (4)  $(\text{La}_{0.6}\text{Sr}_{0.4})_{0.95}\text{Co}_{0.2}\text{Fe}_{0.8}\text{O}_{3-\delta}$ ;<sup>4</sup> 4-probe method (5)  $\text{La}_{0.6}\text{Sr}_{0.4}\text{Co}_{0.2}\text{Fe}_{0.8}\text{O}_{3-\delta}$ ,<sup>5</sup> and (6)  $\text{La}_{0.8}\text{Sr}_{0.2}\text{Co}_{0.8}\text{Fe}_{0.2}\text{O}_{3-\delta}$ ;<sup>6</sup> and oxygen permeation method (7)  $\text{La}_{0.65}\text{Sr}_{0.3}\text{Co}_{0.2}\text{Fe}_{0.8}\text{O}_{3-\delta}$ ,<sup>7</sup> and (8)  $\text{La}_{0.8}\text{Sr}_{0.2}\text{Co}_{0.1}\text{Fe}_{0.9}\text{O}_{3-\delta}$ .<sup>7</sup> Voltage measurement at a fixed temperature on one LSCF sample was performed at a regular interval of 0.259 s for 10 min. Nearly 2.3k data points were averaged for the conductivity determination at a temperature. The error bars represent the standard deviation derived from these nearly 2.3k data points collected at a temperature. The error bars are difficult to see as they are smaller than the size of the symbols.

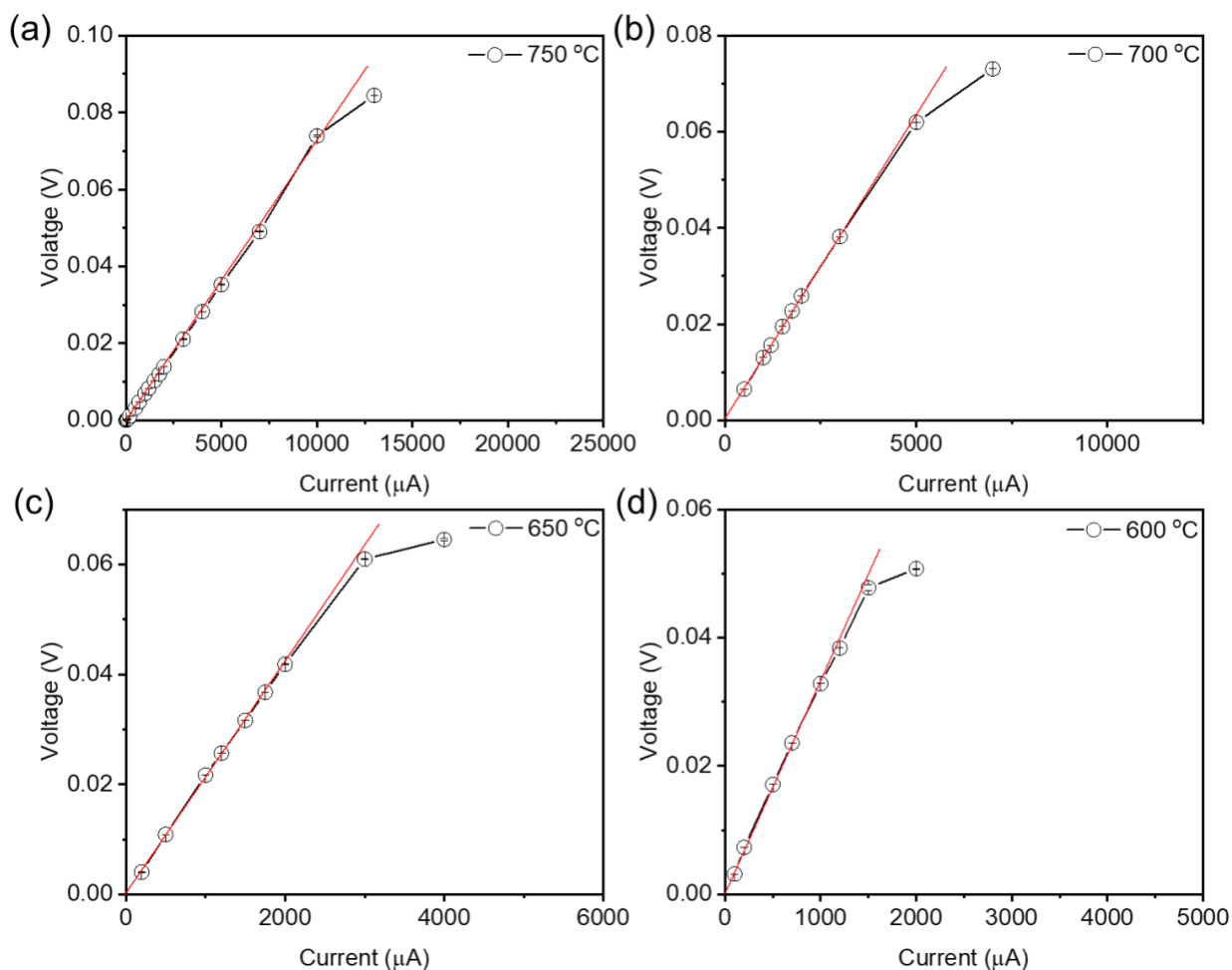


**Figure S12.** Current-voltage characteristics across LMS in one Au/LSCF/YSZ/LMS/LSCF/YSZ/Au system at (a) 750 °C, (b) 700 °C, (c) 650 °C, and (d) 600 °C. The error bars represent the standard deviation obtained from ~150 measurements at each fixed current from one sample. The error bars are difficult to see as they are less than the size of the symbols.

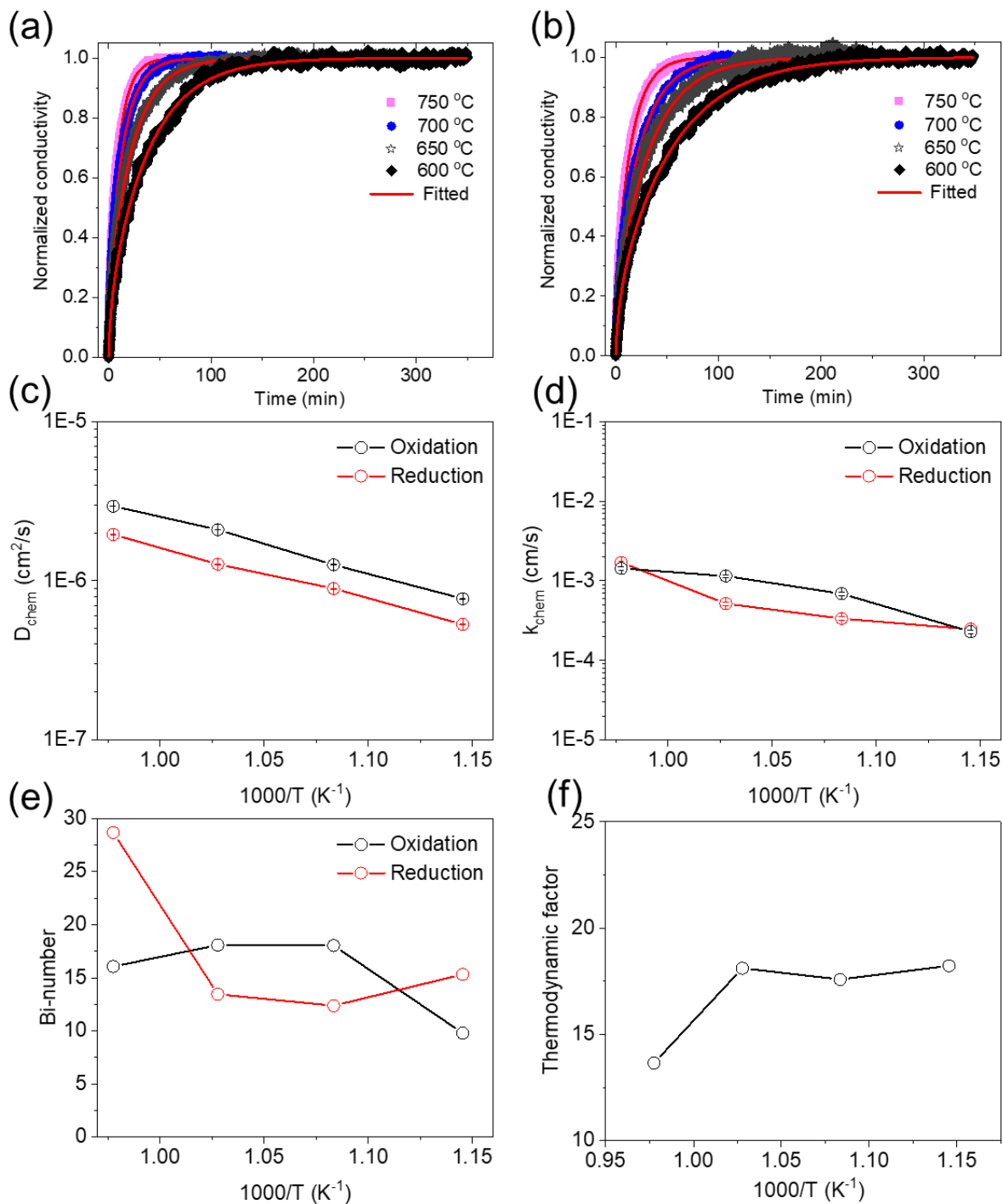


**Figure S13.** Normalized and fitted electrical conductivity relaxation (ECR) data of one LMS sample during the (a) oxidation and (b) reduction at different temperatures. The fitted (c)  $D_{chem}$ , (d)  $k_{chem}$  and (e) calculated Bi-number during oxidation and reduction. (f) Calculated thermodynamic factor at the studied temperatures. The error bars of the fitted values (with 95% confidence, i.e.  $\pm 2$  standard deviation) are smaller than the size of the symbols. Please see details of fitting of the ECR data in Discussion 8.

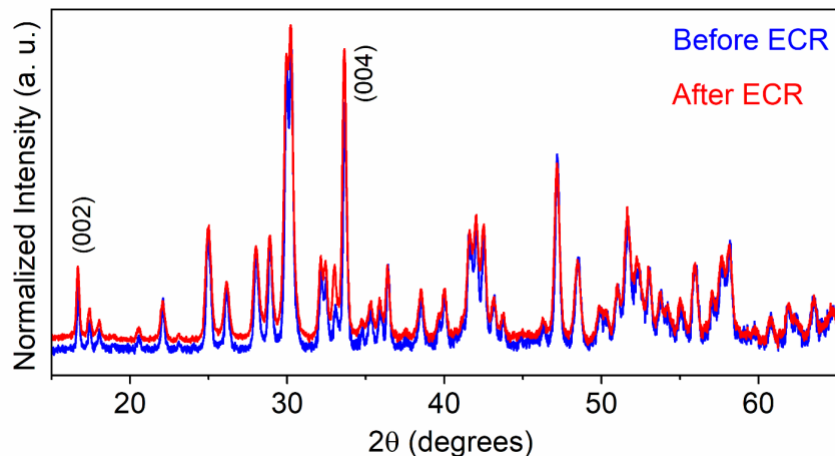


**Figure S14.** Room temperature X-ray diffraction (XRD) pattern of the LMS pellet before and after the electronic conductivity relaxation (ECR) study confirms the structural stability. The XRD profile also demonstrates enhanced grain orientation on the pellet surface along the (001) direction.

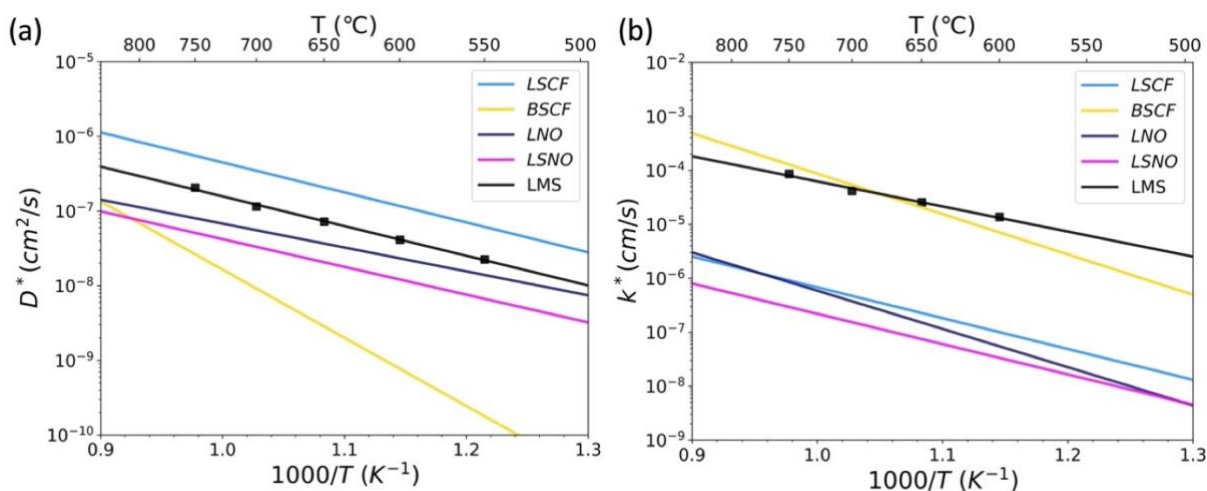


**Figure S15.** (a) The tracer diffusion coefficient  $D^*$  of  $\text{La}_4\text{Mn}_5\text{Si}_4\text{O}_{22+\delta}$  compared with  $\text{La}_{0.6}\text{Sr}_{0.4}\text{Co}_{0.2}\text{Fe}_{0.8}\text{O}_3$  (LSCF),<sup>8–10</sup>  $\text{Ba}_{0.5}\text{Sr}_{0.5}\text{Co}_{0.8}\text{Fe}_{0.2}\text{O}_3$  (BSCF),<sup>11,12</sup>  $\text{La}_2\text{NiO}_{4+\delta}$ ,<sup>13–16</sup> and  $\text{La}_{1.9}\text{Sr}_{0.1}\text{NiO}_{4+\delta}$ .<sup>13,15</sup> (b) The trace surface exchange coefficient  $k^*$  of  $\text{La}_4\text{Mn}_5\text{Si}_4\text{O}_{22+\delta}$  compared with  $\text{La}_{0.6}\text{Sr}_{0.4}\text{Co}_{0.2}\text{Fe}_{0.8}\text{O}_3$  (LSCF),<sup>8,17</sup>  $\text{Ba}_{0.5}\text{Sr}_{0.5}\text{Co}_{0.8}\text{Fe}_{0.2}\text{O}_3$  (BSCF),<sup>11,12</sup>  $\text{La}_2\text{NiO}_{4+\delta}$ ,<sup>13–15,18</sup> and  $\text{La}_{1.9}\text{Sr}_{0.1}\text{NiO}_{4+\delta}$ .<sup>13,15</sup>

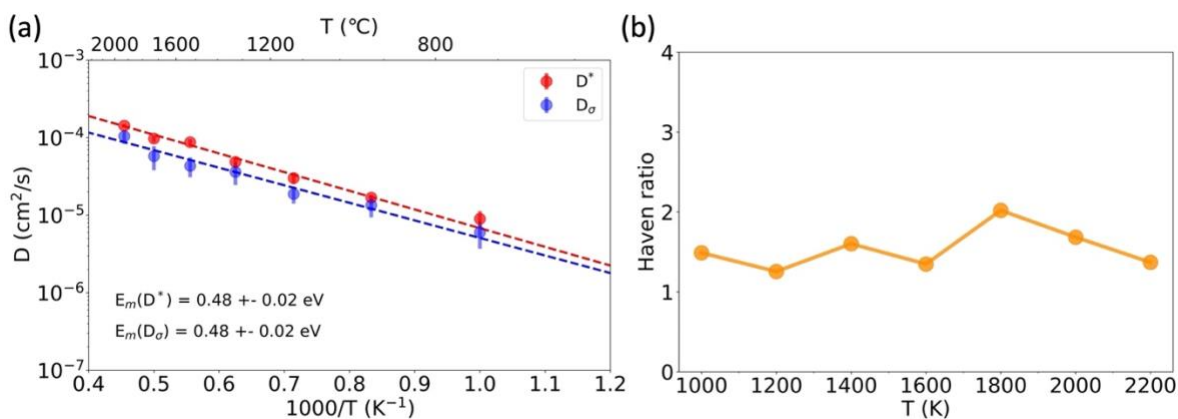


**Figure S16.** (a) Arrhenius plot of tracer diffusion coefficient  $D^*$  and charge diffusion coefficient  $D_\sigma$  of oxygen derived from *ab initio* molecular dynamics (AIMD) with GGA-PBE functional. The error bars represent the standard error of the mean. (b) The Haven ratio calculated by  $D^*$  and  $D_\sigma$  at each temperature.

## Discussion

### 1. Database of experimental migration barrier of oxygen-ion conducting materials.

The compilation of experimental migration barriers for oxygen ion conduction in oxides includes data sourced from the Citrine Informatics ARPA-E Ionics Database,<sup>19</sup> which is the most extensive repository of its kind to our knowledge. Additionally, this collection was enriched with data manually obtained from recent literatures on interstitial oxygen conductors, which were not included in the Citrine database. The Citrine database documented preparation, crystal structure, and properties (such as conductivity and activation energy) for oxygen ion conductors from experimental measurements, including 3039 records with 2340 unique compounds of oxygen ion conductors. Upon a detailed examination of the full database, we collected all materials that displayed results for ionic activation energy, yielding 190 entries of activation energies for vacancy conductors and 14 for interstitial conductors, respectively. The vacancy conductors encompassed various compounds of bismuth oxide, fluorite, LAMOX, perovskites, brownmillerite, and pyrochlore. The interstitial conductors included compounds like apatite and scheelite. This much larger number of vacancy conduction in the database highlights the fact that much less research has been done on interstitial conductors. Our manual literature review added 30 more entries on recently studied interstitial conductors which were not present in the Citrine database, including compounds of apatite, scheelite, Ruddlesden-Popper, hexagonal perovskite, and melilite. The full dataset, including all data extracted from the Citrine database and our additions, and detailing each material's migration barrier and corresponding reference, is available in the supplementary file titled "Experimental ionic migration barrier of oxygen in oxygen-ion conducting oxides.xlsx."

## 2. Origin of the availability of electrons and structural flexibility across families of high-performing interstitial oxygen formers and conductors.

In the following paragraphs, we provide an in-depth examination of our newly discovered and all previously known good interstitial oxygen conducting materials through the lens of these two features and show how these two features enable all of these materials to be good interstitial oxygen formers and conductors. Considering up to the present date but excluding the present work, seven families—apatite,<sup>20</sup> melilite,<sup>21</sup> scheelite,<sup>22</sup> mayenite,<sup>23</sup> Ruddlesden-Popper,<sup>16</sup> hexagonal perovskite,<sup>24,25</sup> and hexagonal manganites<sup>26</sup>—are acknowledged as good interstitial oxygen formers and conductors. Despite other materials like fluorite,<sup>27</sup> corundum,<sup>28</sup> silica,<sup>29</sup> garnet,<sup>30</sup> cuspidine,<sup>31</sup> and langasite<sup>32</sup> having demonstrated some degree of interstitial oxygen diffusion, they are excluded from our list of good interstitial conductors due to either having high oxygen interstitial formation energies ( $E_f=2.2$  eV for corundum  $\text{Cr}_2\text{O}_3$ <sup>28</sup> and  $E_f=1.6$  eV for silica<sup>29</sup>), high oxygen interstitial migration barriers ( $E_a=0.9-1.2$  eV for fluorite  $\text{UO}_{2.08}$ ,<sup>27</sup>  $E_a=1.2$  eV for cuspidine  $\text{La}_4\text{Ga}_2\text{O}_9$ ,<sup>31</sup> and  $E_a=1.1-1.2$  eV for langasite  $\text{La}_3\text{Ga}_{5-x}\text{Ge}_{1+x}\text{O}_{14}$ <sup>32</sup>), or extremely low conductivity ( $\sigma_{ion} \leq 10^{-5}$  S/cm at 800 °C for garnet  $\text{La}_3\text{Ga}_4\text{O}_9$ <sup>30</sup>). A very recent study proposed Te-doped  $\text{LaBi}_2\text{O}_4\text{Cl}$  as a potential new interstitial oxygen conductor<sup>33</sup> but we do not include it in our list of interstitial conductors at this time. Our independent investigation has revealed a complex defect chemistry and vacancy-dominated diffusion mechanisms in this material.<sup>34</sup> We believe more work is needed to establish a robust understanding of its transport mechanisms and assure that it is a proper interstitial oxygen diffuser. Consequently, pure and doped  $\text{LaBi}_2\text{O}_4\text{Cl}$  is excluded from the list. The seven previously known families and the three families discovered in this study gives ten families of established effective interstitial oxygen formers and conductors, all shown in **Fig. 3**.

Available electrons for interstitial oxygen reduction typically come from oxidizable cations or electron donor cation substitution, except for one family, mayenite  $\text{Ca}_{12}\text{Al}_{14}\text{O}_{33}$ , which provides the needed electrons as part of its natural stoichiometry and therefore includes interstitial oxygen as part of the intrinsic stoichiometry and structure of the material. Among the ten families, oxidizable cations contribute available electrons in six families, including  $\text{Mn}^{2+}$  in double molybdates  $\text{K}_2\text{Mn}_2(\text{MoO}_4)_3$ ,  $\text{Mn}^{2+}$  and  $\text{Mn}^{3+}$  in perrierite  $\text{La}_4\text{Mn}_5\text{Si}_4\text{O}_{22}$ ,  $\text{Mn}^{2+}$  in germinates  $\text{CeMn}_2\text{Ge}_4\text{O}_{12}$ ,  $\text{Ni}^{2+}$  in Ruddlesden-Popper  $\text{La}_2\text{NiO}_4$ ,  $\text{Ce}^{3+}$  in scheelite  $\text{CeNbO}_4$ , and  $\text{Mn}^{3+}$  in the hexagonal manganite  $\text{YMnO}_3$ . Available electrons from donor cation substitution occurs in three families, which are  $\text{La}^{3+}$  substitution for  $\text{Sr}^{2+}$  in apatite  $\text{La}_{8.5}\text{Sr}_{1.5}\text{Si}_6\text{O}_{26.25}$ ,<sup>35</sup>  $\text{La}^{3+}$  substitution for  $\text{Sr}^{2+}$  in melilite  $\text{La}_{1.54}\text{Sr}_{0.46}\text{Ga}_3\text{O}_{7.27}$ ,<sup>36</sup> and  $\text{Mo}^{6+}$  substitution for  $\text{Nb}^{5+}$  in hexagonal perovskite  $\text{Ba}_7\text{Nb}_{3.9}\text{Mo}_{1.1}\text{O}_{20.05}$ .<sup>25</sup>

Structural flexibility in these materials is attributed to one of two key structural motifs: (i) corner-sharing polyhedral networks and (ii) isolated polyhedra. The polyhedra in these structural motifs surround small cations (transition and post-transition metals), acting as “network formers” fostering structural connectivity and separated by large cations. These flexible polyhedral structures can both accommodate excess oxygen anion ( $\text{O}_i$ ) and enable their mobility through easy distortion, creating accessible volume and leading to low formation and migration barriers for  $\text{O}_i$  diffusion. To demonstrate these structural aspects more clearly, we categorize the studied

materials based on these two structural motifs and clarify how the two structural motifs facilitate  $O_i$  diffusion.

*i. Corner-sharing polyhedral networks.* Seven structural families contain a corner-sharing polyhedral structural motif, as shown in **Fig. 3(a-g)** in the main text. The corner-sharing polyhedral networks of these materials are Mo tetrahedra and Mn octahedra in  $K_2Mn_2(MoO_4)_3$ , Si tetrahedra and Mn octahedra in  $La_4Mn_5Si_4O_{22}$ , Ge tetrahedra and Mn octahedra in  $CeMn_2Ge_4O_{12}$ , Ni octahedra in  $La_2NiO_4$ , Al tetrahedra in  $Ca_{12}Al_{14}O_{33}$ , 5-fold Mn polyhedra in  $YMnO_3$ , and Ga tetrahedra in  $LaSrGa_3O_7$ , respectively. The interstitial oxygen ( $O_i$ ) diffusion is facilitated by the presence of corner-sharing polyhedral networks for all the materials in this category. Specifically, a common diffusion pathway is that  $O_i$  diffuses through an interstitialcy mechanism by displacing oxygen at the shared corner, which then moves to another interstitial site. This process is aided by the facile rotation of these corner-sharing polyhedra and is the major diffusion mechanism across six structural families. These families include mayenite  $Ca_{12}Al_{14}O_{33}$ ,<sup>37</sup> hexagonal manganite  $YMnO_3$ ,<sup>26</sup> and melilite  $LaSrGa_3O_7$ ,<sup>38</sup> as well as the three new families discovered in this work. (Movies showcasing the diffusion mechanisms of interstitial oxygen ion diffusion in  $La_4Mn_5Si_4O_{22}$ ,  $K_2Mn_2(MoO_4)_3$ , and  $CeMn_2Ge_4O_{12}$  from *ab initio* molecular dynamic simulations, are included in the supplementary files as **Movie S1**, **Movie S2**, and **Movie S3**, respectively.) In Ruddlesden-Popper  $La_2NiO_4$ ,  $O_i$  displaces the apical oxygen of the corner-sharing Ni octahedra, where the soft octahedral rotation mode was found to play a dominant role in  $O_i$  diffusion.<sup>39</sup> The presence of corner-sharing polyhedral networks significantly enhances structural flexibility or softness, exerting a dominant influence on fast interstitial oxygen diffusion. Notably, this structural characteristic is also recognized as advantageous in fast Li-ion conductors.<sup>40,41</sup>

*ii. Isolated polyhedra.* Isolated polyhedra are present in three families, namely hexagonal perovskite  $Ba_7Nb_4MoO_{20}$  with isolated Nb and Mo tetrahedra, apatite  $La_8Sr_2Si_6O_{26}$  with isolated Si tetrahedra, and scheelite  $CeNbO_4$  with isolated Nb tetrahedra in **Fig. 3(h-j)** of the main text. In materials featuring this structural motif,  $O_i$  is stabilized between two nearby tetrahedra, it generally diffuses between these sites (distance  $\approx 4\text{\AA}$ ) along rows of paired tetrahedra through an interstitialcy mechanism with the assistance of tetrahedra rotation. Alternatively,  $O_i$  can diffuse through a pure interstitial mechanism between two more separated tetrahedra pairs (distance  $\approx 5\text{\AA}$ ), where it leaves one tetrahedral pair and passes to another tetrahedral pair. Both the interstitial and interstitialcy mechanisms are observed in apatite families<sup>42-44</sup> and scheelite  $CeNbO_4$ .<sup>22</sup> Interstitialcy diffusion mechanism was observed in hexagonal perovskite family.<sup>25,45</sup> For materials with this structural motif, fast  $O_i$  diffusion is enabled by the rotational flexibility and the dynamical deformation of the isolated tetrahedra.

### 3. Electrical property and defect formation energy with different DFT functionals.

Since the GGA functional predicts underestimated oxygen ion migration barrier and optical band gap compared to the experiments, the band gap and defect formation energy for the bulk structure of  $La_4Mn_5Si_4O_{22+\delta}$  were studied with different DFT exchange and correlation functionals, which are the GGA, GGA with Hubbard U correction (GGA+U) ( $U=3.9\text{eV}$  for Mn),<sup>46</sup> hybrid functional of Heyd, Scuseria, and Ernzerhof (HSE06),<sup>47</sup> and the strongly constrained and appropriately normed (SCAN) functionals.<sup>48</sup> In **Table S3**, we compared the optimized lattice parameters and calculated optical band gap of bulk  $La_4Mn_5Si_4O_{22}$  to both the experimental lattice

parameters from previous research and the band gap measured in our current study. The formation energy of interstitial oxygen varies with different DFT exchange and correlation functionals, from which we believe that different approaches to represent the d-electron physics have a significant effect on the defect formation energies. Based on the performance of different exchange-correlation potentials, SCAN is selected for further studies as it not only accurately predicts geometric lattice parameters and optical band gaps that align with experimental observations but also predicts the oxygen stoichiometry and oxygen conductivity activation energy closely aligned with the experimental observations, as discussed in **Discussion 4** and **Discussion 11** below.

#### 4. DFT studies of oxygen defects in $\text{La}_4\text{Mn}_5\text{Si}_4\text{O}_{22+\delta}$ .

The formation energy of the oxygen interstitial and vacancy (at  $\approx 2\%$  concentration) in the bulk structure of  $\text{La}_4\text{Mn}_5\text{Si}_4\text{O}_{22}$  were calculated under atmospheric conditions ( $T=300\text{ K}$ ,  $P(\text{O}_2)=0.2\text{ atm}$ ). The two most energetically favorable configurations of the interstitial oxygen site were displayed in **Fig. S1a-b** and the most stable configuration of the vacancy oxygen site was shown in **Fig. S1c**, along with the defect formation energies. These calculations were performed using the SCAN functional,<sup>49</sup> which was proven to give the most consistent geometric lattice parameters and band gap value with experiments (**Discussion 3**). Monkhorst–Pack k-point meshes<sup>50</sup> of  $4 \times 3 \times 2$  was used for the  $2 \times 1 \times 1$  supercell with 70 atoms.

The formation energies of  $O_i$  at different concentrations in  $\text{La}_4\text{Mn}_5\text{Si}_4\text{O}_{22+\delta}$  were studied, which are  $-0.11\text{ eV}$ ,  $-0.11\text{ eV}$ ,  $0.49\text{ eV}$ , and  $0.52\text{ eV}$  under air conditions for  $\delta = 0.25, 0.5, 0.75, 1$ , respectively. With including one interstitial oxygen into the  $2 \times 1 \times 1$  supercell ( $\delta = 0.5$ ), the only two  $\text{Mn}^{2+}$  ions in the supercell were oxidized to  $\text{Mn}^{3+}$ . With more interstitial oxygen included ( $\delta = 0.75$ ), the defect formation energy is increased by  $0.6\text{ eV}$ , indicating that further oxidization of  $\text{Mn}^{3+}$  ions is difficult. It is worth noting that the defect formation energies are very close when  $\delta = 0.25, 0.5$  and  $\delta = 0.75, 1$ , respectively, suggesting that the interstitial concentration dependence of the formation energy is much more strongly impacted by the oxidative state of Mn ions than the direct interstitial interaction. The results suggest that the equilibrium concentration of interstitial oxygen in  $\text{La}_4\text{Mn}_5\text{Si}_4\text{O}_{22+\delta}$  is  $\delta \approx 0.5$  under air conditions, which is consistent with the EMPA measurement of the interstitial content  $\delta = 0.42$ .

The *ab initio* studies on the interstitial oxygen concentration in LMS align well with the TGA results, where LMS presents a fairly constant oxygen stoichiometric across a wide range of temperature. These results suggest that the interstitial oxygen is charge balanced by oxidizing  $\text{Mn}^{2+}$  ions and therefore has a concentration highly constrained by the concentration of  $\text{Mn}^{2+}$  ions. When all the  $\text{Mn}^{2+}$  ions are oxidized the interstitial oxygen stoichiometry corresponds to  $\delta = 0.5$ . The TGA and DFT results suggest that, to a good approximation, the material behaviors less like the easily reducible compound  $\text{La}_4\text{Mn}^{4+}_2\text{Mn}^{3+}_{(2+2d)}\text{Mn}^{2+}_{(1-2d)}\text{O}_{22+\delta}$  and more like the stoichiometry compound  $\text{La}_4\text{Mn}^{4+}_2\text{Mn}^{3+}_3\text{O}_{22+0.5}$ .

#### 5. Calculated spin state of $\text{La}_4\text{Mn}_5\text{Si}_4\text{O}_{22+\delta}$ .

The DFT calculated magnetic moments are consistent with  $\text{Mn}_1^{4+}$ ,  $\text{Mn}_2^{3+}$  and  $\text{Mn}_3^{2+}$  being in their high spin magnetic states. More specifically, our average integrated (within the Wigner-Seitz radius) z-component of the spin on  $\text{Mn}_1$ ,  $\text{Mn}_2$ , and  $\text{Mn}_3$  are  $2.90$ ,  $3.41$ , and  $4.41\ \mu_B$  from DFT GGA-PBE calculation, respectively. These values are consistent with the expected ideal formal

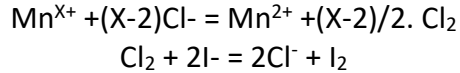
valence spin state based on summing of unpaired electrons of 3, 4, and 5 for  $Mn_1^{4+}$ ,  $Mn_2^{3+}$  and  $Mn_3^{2+}$ , respectively. These ideal formal valence spin values can be used to calculate the total spin-only magnetic moment from the formula  $\mu_{cal}^2 = 2 * \mu_{cal}^2(Mn^{4+}) + 2 * \mu_{cal}^2(Mn^{3+}) + \mu_{cal}^2(Mn^{2+})$  /formula unit,<sup>1</sup> where for each Mn ion the effective magnetic moment was calculated by  $\mu_{cal} = \sqrt{n * (n + 2)}$  and  $n$  is the sum of unpaired electron. Using this formula, the total spin-only magnetic moment is predicted to be  $10.63 \mu_B$ /formula unit, which is an excellent match for the experimental measured value of  $10.64 \mu_B$ /formula.<sup>1</sup> Upon the inclusion of  $O_i$ , two adjacent  $Mn^{2+}$  ions are oxidized to  $Mn^{3+}$ , with a change of the spin state from 5 to 4.

## 6. Climbing Image Nudged Elastic Band (CI-NEB) calculation.

The migration barriers of the  $O_i$  interstitial and interstitialcy diffusion pathways in LMS were studied by the Climbing Image Nudged Elastic Band (CI-NEB) method.<sup>51</sup> The calculations were performed separately using GGA-PBE and SCAN functionals. The plane wave cutoff energy was set as 520 eV. The stopping criteria for total energy calculations were 0.001 meV/cell for electronic relaxation and 0.05 eV/Å for ionic relaxation, respectively. 7 images were used for the interstitial diffusion pathway and 5 images were used for the interstitialcy diffusion pathway.

## 7. Iodometric titration.

Iodometric titration was performed in nitrogen atmosphere based on the following assumptions/criteria: First, charge neutrality; second, cations are in the stoichiometric ratio as obtained in the EPMA study; third, the valence of La and Si in LMS is 4+; fourth, average valence of Mn in LMS is  $X+ > 2+$ . The reaction mechanism is



A weighed amount of ground LMS pellet was dissolved in an aqueous solution of KI and HCl (6N).  $Cl_2$  is generated during this dissolution and the in-situ generated  $Cl_2$  reacts with the  $I^-$  to produce  $I_2$ . The liberated  $I_2$  is measured by titration with a standard volumetric aqueous solution of  $Na_2S_2O_3$  (~ 0.01 N). Finally, the stoichiometry of the oxygen was calculated from the measured  $I_2$  amount. The measurement was repeated for five times to confirm the reproducibility, and the average value along with the standard deviation in the mean was presented in **Table S6**.

## 8. Preparation of the ionic conductivity measurement using YSZ blocks.

The ionic conductivity measurement was performed using pre-synthesized commercial electrode material yttria-stabilized zirconia (8 mol %  $Y_2O_3$  in  $ZrO_2$ , 8YSZ; Sigma Aldrich) blocks as the electronic blocking electrode.<sup>4</sup> The 8YSZ pellets were sintered at 1500 °C for 6 hours. As shown in **Figure S10**, the cross-section of the 8YSZ pellets was 4.8 mm x 4.8 mm and the thickness was 1.5 mm. The thickness of the LMS pellets were ~ 0.8 mm. All pellets were polished on all sides to remove any surface contamination and to reduce contact resistance. To ensure better connectivity between LMS and 8YSZ pellet we used a homemade paste of LMS in ethanol and made a thin layer of LMS between LMS and 8YSZ blocks. For voltage measurement, two thin Au wires were inserted at the YSZ and LMS junctions for the voltage measurement. To measure the voltage across the LMS pellet accurately, we sputtered an Au line (width ~ 0.2 mm, thickness ~ 200 nm) on the LMS surface and connected it with the Au wires. For the efficient oxygen exchange, we used two porous LSCF pellets (thickness ~ 1 mm) at two ends of the assembly. The porous LSCF pellets were sintered at 1050 °C for 6 hours using commercial LSCF electrode power (Sigma Aldrich). These two sintered porous LSCF pellets were also connected to the YSZ pellet by

a thin LSCF layer made using homemade LSCF paste. The exposed surface of the LSCF pellets was coated with Au by sputtering. The whole sample assembly was pressed vertically between two Au-coated alumina plates and two Pt wires were connected to these alumina plates as the current leads. The whole system was sintered at 900 °C for 1 hour before performing the measurement.

### 9. Fitting of the ECR data

The obtained ECR data was fitted to determine the  $D_{chem}$ ,  $k_{chem}$  along with its standard deviation in the average value, using a previous reported 2-D model.<sup>52</sup> In **Figure S13(a, b)**, the non-linear least square fitting was performed using the publicly available NETL Electrical Conductivity Relaxation (ECR) Analysis Tool.<sup>52</sup> A small conductivity drift was observed during the whole ECR process which may happen due to the microstructure change occurring at high temperatures. We corrected this resistance drift before fitting. The ECR data shown a very fast oxygen exchange at the beginning (~30 s to 2 min, with the time being inversely proportional to temperature) of the transient response, which may be due to the presence of (001) oriented grain on the pellet surface (confirmed by XRD, **Figure S14**) or a patch of unknown secondary surface phase sufficiently thin as to not be detectable by XRD. In order to fit the ECR data using a single phase model, we neglected this fast response region as fitting this region using the single phase model gives a very high value of  $k_{chem}$  with a large error bar. We have chosen the initial point where the percentage of error in both  $D_{chem}$  and  $k_{chem}$  is < 5%. The error bars reported for the  $D_{chem}$  and  $k_{chem}$  represent a 95% confidence interval for  $D_{chem}$  and  $k_{chem}$  that is provided as part of the NETL ECR Analysis Tool<sup>52</sup> based on numerical aspects of their fitting. However, it is important to acknowledge that the true uncertainty in the values of  $D_{chem}$  and  $k_{chem}$  can be affected by many issues, including sample to sample variability,  $D_{chem}$  and  $k_{chem}$  covariance in fitting<sup>52</sup> and multiple measurement limitations, e.g., gas flush effects.<sup>53</sup> Variations in  $D_{chem}$  and  $k_{chem}$  between different samples, research groups, and experimental setups and approaches are often close to an order of magnitude, even for well-studied materials. The value of  $D_{chem}$  and  $k_{chem}$  of LMS at a fixed temperature was determined as the average during oxidation and reduction at that temperature. The potential for reliable determination of both  $D_{chem}$  and  $k_{chem}$  was confirmed by the Bi-number, defined as  $Bi = \frac{L_z}{D_{chem}/k_{chem}}$ , where  $L_z$  represents the half-thickness of the LMS sample. The obtained values of Bi number falls within the range of 0.03 to 30<sup>54</sup> (**Figure S13e**), suggesting that reliable values of both  $D_{chem}$  and  $k_{chem}$  can be extracted from the measurement. The stability of the samples after the ECR measurement was confirmed using the XRD technique (**Figure S14**).

### 10. Determination of average $D_{chem}$ and $k_{chem}$ of state-of-art materials from literatures.

Diffusion coefficient  $D$  and surface exchange coefficient  $k$  of  $\text{La}_4\text{Mn}_5\text{Si}_4\text{O}_{22+\delta}$  were compared with state-of-the-art materials  $\text{La}_{0.6}\text{Sr}_{0.4}\text{Co}_{0.2}\text{Fe}_{0.8}\text{O}_{3-\delta}$  (LSCF),  $\text{Ba}_{0.5}\text{Sr}_{0.5}\text{Co}_{0.8}\text{Fe}_{0.2}\text{O}_{3-\delta}$  (BSCF),  $\text{La}_{0.5}\text{Sr}_{0.5}\text{CoO}_{3-\delta}$  (LSC),  $\text{La}_{0.5}\text{Sr}_{0.5}\text{FeO}_{3-\delta}$  (LSF),  $\text{BaCoFeYO}_{3-\delta}$  (BCFY), and  $\text{La}_2\text{NiO}_{4+\delta}$  (**Fig. 4(e,f) and Figure S15**). Data along with references are available as digital SI. and We found that there is a wide variation of the  $D$  and  $k$  reported at different temperatures, making the comparison difficult. Hence, we have calculated the average of  $D$  and  $k$  at 600 °C and 800 °C from the literatures where the authors have studied at least two different temperatures. From the average  $D$  and  $k$ , we determined the activation energy using the Arrhenius relationship and derived  $D$  and  $k$  changing with temperature.

## 11. Conversion of *ab initio* diffusivity to conductivity and derivation of Haven ratio.

We performed a detailed analysis comparing ionic conductivity predicted by DFT studies to the experimental measurements. We intend to base these results on migration barriers calculated by DFT-SCAN, which is the best functional that accurately predicts properties of LMS. Hence, the DFT predicted conductivity was determined by

$$\sigma T = A_\sigma e^{\left(-\frac{E_A}{k_b T}\right)} \quad (\text{Eq. S1}),$$

where  $T$  is temperature, and  $k_b$  is the Boltzmann constant. Given there is almost no temperature dependence of oxygen stoichiometry from TGA, the DFT results suggesting oxygen stoichiometry is largely pinned by the amount of  $\text{Mn}^{2+}$  ions, and the consistency of interstitial oxygen content from DFT with the experimental stoichiometries from EPMA,  $E_A$  is expected to be close  $E_m$ . Hence we use our DFT-SCAN results to set  $E_A \approx E_m = \frac{1}{2}(0.69 \text{ eV} + 0.74 \text{ eV}) = 0.715 \text{ eV}$ . The prefactor  $A_\sigma$  is obtained based on the GGA-PBE AIMD simulations as SCAN is too expensive for long-time AIMD studies. Given that the prefactor  $A_\sigma$  enters the expression for  $\sigma$  linearly, unlike the exponential dependence on  $E_A$ , employing GGA-PBE AIMD data for  $A_\sigma$  is considered to introduce minimal errors in the estimation of  $\sigma$ .

Below we describe the process of obtaining  $A_\sigma$  by converting GGA-PBE AIMD diffusivity to conductivity and introduce the Haven ratio. The conversion between diffusivity and conductivity can be achieved through the Nernst-Einstein relation <sup>55</sup>

$$\sigma = \left(\frac{cz^2F^2}{RT}\right) D_\sigma \quad (\text{Eq. S2}),$$

where  $\sigma$  is the conductivity,  $R$  is gas constant,  $T$  is temperature,  $c$  is the oxygen volume concentration calculated as  $c = \frac{22+\delta}{V}$ , where  $\delta = 0.42$ . Additionally,  $z$  is the charge of oxygen ion (-2), and  $F$  is the faraday constant.  $D_\sigma$  is a derived quantity called the charge diffusion coefficient, although it is also referred to as a self-diffusion coefficient or jump diffusion coefficient in different studies. The  $D_\sigma$  is correlated to the tracer diffusion coefficient  $D^*$  through the Haven ratio  $H_R = \frac{D^*}{D_\sigma}$ . So, **Eq. S2** can be rewritten as

$$\sigma = \left(\frac{cz^2F^2}{RT}\right) \frac{D^*}{H_R} \quad (\text{Eq. S3}).$$

Below we describe the calculation process of  $H_R$ . It has been shown that  $D_\sigma$  can be calculated from the mean square displacement of center of mass of all diffusers,<sup>56</sup> as inserting this form of  $D_\sigma$  to Nernst-Einstein equation is equivalent to using the Green–Kubo expression for determining the ionic conductivity  $\sigma$ .<sup>57</sup> we calculated the tracer diffusion coefficient  $D^*$  and the charge diffusion coefficient  $D_\sigma$  using the GGA-PBE AIMD simulations using the following equations

$$D^* = \frac{1}{2dt} \left\langle \frac{1}{N} \sum_{i=1}^N \langle [\vec{r}_i(t)]^2 \rangle \right\rangle \quad (\text{Eq. S4}),$$

$$D_\sigma = \frac{1}{2dt} \left\langle \frac{1}{N} \left( \sum_{i=1}^N \vec{r}_i(t) \right)^2 \right\rangle \quad (\text{Eq. S5}),$$

where  $N$  is the number of diffusing ions,  $\vec{r}_i(t)$  is the displacement of the  $i$ th ion after time  $t$ ,  $d$  is the dimension. Note that we here obtain the 3D diffusivity using  $d = 3$  to convert to conductivity.  $\langle [\vec{r}_i(t)]^2 \rangle$  is the mean square displacement of the  $i$ th diffuser after time  $t$ ,  $\langle (\sum_{i=1}^N \vec{r}_i(t))^2 \rangle$  is the mean square displacement of the center of mass of all diffusers after time  $t$ . **Figure S16a** shown that  $D^*$  and  $D_\sigma$  are in the same order and present consistent migration barriers derived through fitting the Arrhenius relation  $D = D_0 e^{(-\frac{E_m}{k_b T})}$ . Our results yielded a consistent and nearly constant Haven ratio ( $H_R = 1.54 \pm 0.24$ , as shown in **Figure S16b**) across all studied temperatures. The smaller error bars for  $D^*$  suggested that the measurements of  $D^*$  from AIMD simulation are more precise than  $D_\sigma$ , and the latter usually requires much longer simulation time. So the GGA-PBE  $D^*$  is converted to conductivity by **Eq. S3** using  $H_R = 1.54$ . Finally, we performed the Arrhenius relation fitting (**Eq. S1**) to the GGA-PBE predicted  $\sigma$  and obtained the prefactor  $A_\sigma = 2.68 \times 10^5 \text{ S/cm} \cdot \text{K}$ . This  $A_\sigma$  value is then used in Eq. S1 with the DFT-SCAN  $E_A = 0.715 \text{ eV}$  derived above to predict a DFT conductivity for comparison to experiment.

In **Fig. 4c**, we present the DFT conductivity compared to the experimental data. The comparison demonstrates that the experimental ionic conductivity closely aligns with the results from the DFT simulations, supporting that we are calculating the correct mechanisms governing the measured conductivity.

## Reference

1. Gueho, C., Giaquinta, D., Mansot, J. L., Ebel, T. & Palvadeau, P. Structure and Magnetism of  $\text{La}_4\text{Mn}_5\text{Si}_4\text{O}_{22}$  and  $\text{La}_4\text{V}_5\text{Si}_4\text{O}_{22}$ : Two New Rare-Earth Transition Metal Sorosilicates. *Chem. Mater.* **7**, 486–492 (1995).
2. Cacciuttolo, Q., Vulliet, J., Lair, V., Cassir, M. & Ringuedé, A. Influence of pressure on the electrical and electrochemical behaviour of high-temperature steam electrolyser  $\text{La}_{0.6}\text{Sr}_{0.4}\text{Co}_{0.2}\text{Fe}_{0.8}\text{O}_3$  anode. *J. Solid State Electrochem.* **22**, 3663–3671 (2018).
3. Fan, B., Yan, J. & Yan, X. The ionic conductivity, thermal expansion behavior, and chemical compatibility of  $\text{La}_{0.54}\text{Sr}_{0.44}\text{Co}_{0.2}\text{Fe}_{0.8}\text{O}_{3-\delta}$  as SOFC cathode material. *Solid State Sci.* **13**, 1835–1839 (2011).
4. Lei, C., Simpson, M. F. & Virkar, A. V. Investigation of Ion and Electron Conduction in the Mixed Ionic-Electronic Conductor- La-Sr-Co-Fe-Oxide (LSCF) Using Alternating Current (AC) and Direct Current (DC) Techniques. *J. Electrochem. Soc.* **169**, 14506 (2022).
5. Teraoka, Y., Nobunaga, T., Okamoto, K., Miura, N. & Yamazoe, N. Influence of constituent metal cations in substituted  $\text{LaCoO}_3$  on mixed conductivity and oxygen permeability. *Solid State Ion.* **48**, 207–212 (1991).
6. Teraoka, Y., Zhang, H. M., Okamoto, K. & Yamazoe, N. Mixed ionic-electronic conductivity of  $\text{La}_{1-x}\text{Sr}_x\text{Co}_{1-y}\text{Fe}_y\text{O}_{3-\delta}$  perovskite-type oxides. *Mater. Res. Bull.* **23**, 51–58 (1988).
7. Ullmann, H., Trofimenko, N., Tietz, F., Stöver, D. & Ahmad-Khanlou, A. Correlation between thermal expansion and oxide ion transport in mixed conducting perovskite-type oxides for SOFC cathodes. *Solid State Ion.* **138**, 79–90 (2000).
8. Armstrong, E. N., Duncan, K. L. & Wachsman, E. D. Effect of A and B-site cations on surface exchange coefficient for  $\text{ABO}_3$  perovskite materials. *Phys. Chem. Chem. Phys.* **15**, 2298–2308 (2013).

9. Li, Y., Gerdes, K., Horita, T. & Liu, X. Surface Exchange and Bulk Diffusivity of LSCF as SOFC Cathode: Electrical Conductivity Relaxation and Isotope Exchange Characterizations. *J. Electrochem. Soc.* **160**, F343 (2013).
10. Armstrong, E. N., Duncan, K. L., Oh, D. J., Weaver, J. F. & Wachsman, E. D. Determination of Surface Exchange Coefficients of LSM, LSCF, YSZ, GDC Constituent Materials in Composite SOFC Cathodes. *J. Electrochem. Soc.* **158**, B492 (2011).
11. Wang, L., Merkle, R., Maier, J., Acartürk, T. & Starke, U. Oxygen tracer diffusion in dense  $\text{Ba}_{0.5}\text{Sr}_{0.5}\text{Co}_{0.8}\text{Fe}_{0.2}\text{O}_{3-\delta}$  films. *Appl. Phys. Lett.* **94**, 71908 (2009).
12. Berenov, A. *et al.* Oxygen tracer diffusion and surface exchange kinetics in  $\text{Ba}_{0.5}\text{Sr}_{0.5}\text{Co}_{0.8}\text{Fe}_{0.2}\text{O}_{3-\delta}$ . *Solid State Ion.* **268**, 102–109 (2014).
13. Skinner, S. J. & Kilner, J. A. Oxygen diffusion and surface exchange in  $\text{La}_{2-x}\text{Sr}_x\text{NiO}_{4+\delta}$ . *Solid State Ion.* **135**, 709–712 (2000).
14. Kilner, J. A. & Shaw, C. K. M. Mass transport in  $\text{La}_2\text{Ni}_{1-x}\text{Co}_x\text{O}_{4+\delta}$  oxides with the  $\text{K}_2\text{NiF}_4$  structure. *Solid State Ion.* **154**, 523–527 (2002).
15. Skinner, S. J. & Kilner, J. A. A comparison of the transport properties of  $\text{La}_{2-x}\text{Sr}_x\text{Ni}_{1-y}\text{Fe}_y\text{O}_{4+\delta}$  where  $0 < x < 0.2$  and  $0 < y < 0.2$ . *Ionics* **5**, 171–174 (1999).
16. Song, J., Ning, D., Boukamp, B., Bassat, J. M. & Bouwmeester, H. J. M. Structure, electrical conductivity and oxygen transport properties of Ruddlesden-Popper phases  $\text{Ln}_{n+1}\text{Ni}_n\text{O}_{3n+1}$  ( $\text{Ln} = \text{La}, \text{Pr}$  and  $\text{Nd}$ ;  $n = 1, 2$  and  $3$ ). *J. Mater. Chem. A* **8**, 22206–22221 (2020).
17. Saher, S. *et al.* Influence of ionic conductivity of the nano-particulate coating phase on oxygen surface exchange of  $\text{La}_{0.58}\text{Sr}_{0.4}\text{Co}_{0.2}\text{Fe}_{0.8}\text{O}_{3-\delta}$ . *J. Mater. Chem. A* **5**, 4991–4999 (2017).
18. Song, C., Yi, J. & Yan, Y. Detailed description of pulse isotopic exchange method for analyzing oxygen surface exchange behavior on oxide ion conductors. *Chinese Journal of Chemical Physics* **32**, 474–484 (2019).
19. Antono, E., Meredig, B., & Mulholland, G. J. Citrine Informatics ARPA-E Ionics Database. <https://citrination.com/datasets/151085> (accessed August 18).
20. Nakayama, S., Kageyama, T., Aono, H. & Sadaokac, Y. Ionic Conductivity of Lanthanoid Silicates,  $\text{Ln}_{10}(\text{SiO}_4)_6\text{O}_3$  ( $\text{Ln} = \text{La}, \text{Nd}, \text{Sm}, \text{Gd}, \text{Dy}, \text{Y}, \text{Ho}, \text{Er}$  and  $\text{Yb}$ ). *J. Mater. Chem.* **5**, 1801–1805 (1995).
21. Kuang, X. *et al.* Interstitial oxide ion conductivity in the layered tetrahedral network melilite structure. *Nat. Mater.* **7**, 498–504 (2008).
22. Li, J. *et al.* Modulated structure determination and ion transport mechanism of oxide-ion conductor  $\text{CeNbO}_{4+\delta}$ . *Nat. Commun.* **11**, 1–9 (2020).
23. Lacerda M. *et al.* High oxide ion conductivity in  $\text{Ca}_{12}\text{Al}_{14}\text{O}_{33}$ . *Nature* **332**, 525–526 (1988).
24. Fop, S. *et al.* High oxide ion and proton conductivity in a disordered hexagonal perovskite. *Nat. Mater.* **19**, 752–757 (2020).
25. Yashima, M. *et al.* High oxide-ion conductivity through the interstitial oxygen site in  $\text{Ba}_7\text{Nb}_4\text{MoO}_{20}$ -based hexagonal perovskite related oxides. *Nat. Commun.* **12**, 1–7 (2021).
26. Skjærvø, S. H. *et al.* Interstitial oxygen as a source of p-type conductivity in hexagonal manganites. *Nat. Commun.* **7**, 7491 (2016).
27. Murch, G. E., Bradhurst, D. H. & De Bruin, J. H. Oxygen self-diffusion in non-stoichiometric uranium dioxide. *Philosophical Magazine* **32**, 1141–1150 (1975).

28. Medasani, B., Sushko, M. L., Rosso, K. M., Schreiber, D. K. & Bruemmer, S. M. First-Principles Investigation of Native Interstitial Diffusion in Cr<sub>2</sub>O<sub>3</sub>. *J. Phys. Chem. C* **122**, 12984–12993 (2018).
29. Roma, G., Limoge, Y. & Baroni, S. Oxygen self-diffusion in  $\alpha$ -quartz. *Phys. Rev. Lett.* **86**, 4564–4567 (2001).
30. Yasui, Y., Niwa, E., Matsui, M., Fujii, K. & Yashima, M. Discovery of a Rare-Earth-Free Oxide-Ion Conductor Ca<sub>3</sub>Ga<sub>4</sub>O<sub>9</sub> by Screening through Bond Valence-Based Energy Calculations, Synthesis, and Characterization of Structural and Transport Properties. *Inorg. Chem.* **58**, 9460–9468 (2019).
31. Martín-Sedeño, M. C. *et al.* Enhancement of oxide ion conductivity in cuspidine-type materials. *Chem. Mater.* **16**, 4960–4968 (2004).
32. Diaz-Lopez, M. *et al.* Interstitial Oxide Ion Conductivity in the Langasite Structure: Carrier Trapping by Formation of (Ga,Ge)<sub>2</sub>O<sub>8</sub> Units in La<sub>3</sub>Ga<sub>5-x</sub>Ge<sub>1+x</sub>O<sub>14+x/2</sub> (0 < x ≤ 1.5). *Chem. Mater.* **31**, 5742–5758 (2019).
33. Yaguchi, H., Morikawa, D., Saito, T., Tsuda, K. & Yashima, M. High Oxide-Ion Conductivity through the Interstitial Oxygen Site in Sillén Oxychlorides. *Adv. Funct. Mater.* **33**, 214082. (2023).
34. Meng, J, *et al.* Discovery of New Fast Oxygen Conductors: Bi<sub>2</sub>MO<sub>4</sub>X (M= rare earth, X= halogen) Via Unsupervised Machine Learning. in *243rd ECS Meeting with the 18th International Symposium on Solid Oxide Fuel Cells (SOFC-XVIII)* (2023).
35. Zhang, Y., Su, Z., Azad, A. K., Zhou, W. & Irvine, J. T. S. Directly imaging interstitial oxygen in silicate apatite. *Adv. Energy Mater.* **2**, 316–321 (2012).
36. Thomas, C. I. *et al.* Phase stability control of interstitial oxide ion conductivity in the La<sub>1+x</sub>Sr<sub>1-x</sub>Ga<sub>3</sub>O<sub>7+x/2</sub> Melilite Family. *Chem. Mater.* **22**, 2510–2516 (2010).
37. Hosono, H., Hayashi, K., Kajihara, K., Sushko, P. V. & Shluger, A. L. Oxygen ion conduction in 12CaO·7Al<sub>2</sub>O<sub>3</sub>: O<sup>2-</sup>- conduction mechanism and possibility of O<sup>-</sup>- fast conduction. *Solid State Ion.* **180**, 550–555 (2009).
38. Schuett, J., Schultze, T. K. & Grieshammer, S. Oxygen Ion Migration and Conductivity in LaSrGa<sub>3</sub>O<sub>7</sub> Melilites from First Principles. *Chem. Mater.* **32**, 4442–4450 (2020).
39. Li, X. & Benedek, N. A. Enhancement of ionic transport in complex oxides through soft lattice modes and epitaxial strain. *Chem. Mater.* **27**, 2647–2652 (2015).
40. Muy, S., Schlem, R., Shao-Horn, Y. & Zeier, W. G. Phonon–Ion Interactions: Designing Ion Mobility Based on Lattice Dynamics. *Adv. Energy Mater.* **11**, 1–14 (2021)
41. Jun, K. J. *et al.* Lithium superionic conductors with corner-sharing frameworks. *Nat. Mater.* **21**, 924-931. (2022).
42. Schultze, T. K., Arnold, J. P. & Grieshammer, S. Ab Initio Investigation of Migration Mechanisms in la Apatites. *ACS Appl. Energy Mater.* **2**, 4708–4717 (2019).
43. Imaizumi, K., Toyoura, K., Nakamura, A. & Matsunaga, K. Cooperative oxide-ion conduction in apatite-type lanthanum germanate-A first principles study. *J. Ceram. Soc. Jpn.* **125**, 105–111 (2017).
44. Panchmatia, P. M. *et al.* Oxygen Defects and Novel Transport Mechanisms in Apatite Ionic Conductors: Combined 17O NMR and Modeling Studies. *Angew. Chem.* **123**, 9500–9505 (2011).

45. Yasui, Y., Tsujiguchi, T., Sakuda, Y., Hester, J. R. & Yashima, M. Oxide-Ion Occupational Disorder, Diffusion Path, and Conductivity in Hexagonal Perovskite Derivatives  $\text{Ba}_3\text{WNbO}_{8.5}$  and  $\text{Ba}_3\text{MoNbO}_{8.5}$ . *J. Phys. Chem. C* **126**, 2383–2393 (2022).
46. Anisimov, V. I., Zaanen, J. & Andersen, O. K. Band theory and Mott insulators: Hubbard U instead of Stoner I. *Phys. Rev. B* **44**, 943–954 (1991).
47. Heyd, J., Scuseria, G. E. & Ernzerhof, M. Hybrid functionals based on a screened Coulomb potential. *J. Chem. Phys.* **118**, 8207–8215 (2003).
48. Sun, J., Ruzsinszky, A. & Perdew, J. Strongly Constrained and Appropriately Normed Semilocal Density Functional. *Phys. Rev. Lett.* **115**, 1–6 (2015).
49. Perdew, J. P., Burke, K. & Wang, Y. Generalized gradient approximation for the exchange-correlation hole of a many-electron system. *Phys. Rev. B* **54**, 16533–16539 (1996).
50. Monkhorst, H. J. & Pack, J. D. Special points for Brillouin-zone integrations. *Phys. Rev. B* **13**, 5188–5192 (1976).
51. Henkelman, G., Uberuaga, B. P. & Jónsson, H. A climbing image nudged elastic band method for finding saddle points and minimum energy paths. *J. Chem. Phys.* **113**, 9901–9904 (2000).
52. Na, B. T. *et al.* Enhanced accuracy of electrochemical kinetic parameters determined by electrical conductivity relaxation. *Solid State Ion.* **361**, 115561 (2021).
53. den Otter, M. W., Bouwmeester, H. J. M., Boukamp, B. A. & Verweij, H. Reactor Flush Time Correction in Relaxation Experiments. *J. Electrochem. Soc.* **148**, J1 (2001).
54. Song, J., Ning, D., Boukamp, B., Bassat, J.-M. & Bouwmeester, H. J. M. Structure, electrical conductivity and oxygen transport properties of Ruddlesden–Popper phases  $\text{Ln}_{n+1}\text{Ni}_n\text{O}_{3n+1}$  (Ln = La, Pr and Nd; n = 1, 2 and 3). *J. Mater. Chem. A* **8**, 22206–22221 (2020).
55. Murch, G. E. The Haven ratio in fast ionic conductors. *Solid State Ion.* **7**, 177–198 (1982).
56. der Ven, A., Ceder, G., Asta, M. & Tapesch, P. D. First-principles theory of ionic diffusion with nondilute carriers. *Phys. Rev. B* **64**, 184307 (2001).
57. Uebing, C. & Gomer, R. Determination of surface diffusion coefficients by Monte Carlo methods: Comparison of fluctuation and Kubo–Green methods. *J. Chem. Phys.* **100**, 7759–7766 (1994).